



저작자표시-비영리-변경금지 2.0 대한민국

이용자는 아래의 조건을 따르는 경우에 한하여 자유롭게

- 이 저작물을 복제, 배포, 전송, 전시, 공연 및 방송할 수 있습니다.

다음과 같은 조건을 따라야 합니다:



저작자표시. 귀하는 원저작자를 표시하여야 합니다.



비영리. 귀하는 이 저작물을 영리 목적으로 이용할 수 없습니다.



변경금지. 귀하는 이 저작물을 개작, 변형 또는 가공할 수 없습니다.

- 귀하는, 이 저작물의 재이용이나 배포의 경우, 이 저작물에 적용된 이용허락조건을 명확하게 나타내어야 합니다.
- 저작권자로부터 별도의 허가를 받으면 이러한 조건들은 적용되지 않습니다.

저작권법에 따른 이용자의 권리는 위의 내용에 의하여 영향을 받지 않습니다.

이것은 [이용허락규약\(Legal Code\)](#)을 이해하기 쉽게 요약한 것입니다.

[Disclaimer](#)

공학박사 학위논문

Topology Optimization: Path Planning and Variational Art

위상 최적화: 경로 계획 및 변분 미술

2012년 8월

서울대학교 대학원
공과대학 기계항공공학부
류재춘

Abstract
Topology Optimization:
Path Planning and Variational Art

Jaechun Ryu

The School of Mechanical and Aerospace Engineering

The Graduate School

Seoul National University

This thesis deals with two independent topics. The first is the global path planning algorithm of a mobile robot. And the second is the variational art algorithm.

For the first topic, the path planning problem for a mobile robot moving in a planned environment filled with obstacles is addressed. The approach is based on the principle of thermal conduction and structural topology optimization and rests on the observation that, by identifying the starting and ending configurations of a mobile robot as the heat source and sink of a conducting plate, respectively, the path planning problem can be formulated as a topology optimization problem that minimizes thermal compliance. Obstacles are modeled as regions of zero thermal conductivity; in fact, regions can be assigned varying levels of non-uniform conductivity depending on the application. The feasibility and practicality of the approach is validated through numerical examples; the indoor path planning problems and the outdoor path planning problems in various conditions will be solved.

For the second topic, this thesis presents computer-aided aesthetic design

referred as a variational art by using topology optimization method based on the variational principle. It bears some similarity with painting or drawing in a blank canvas in art. To realize aesthetic design by topology optimization method, activities drawing a line and plane are considered as finding an optimal path connecting heat source and sink on a two-dimensional heat-conducting plate under a mass constraint. There are several parameters controlling images to be produced. The effects of various parameters will be studied. In addition, some representative artworks obtained by the proposed approach will be presented.

Keywords: Topology Optimization, Heat transfer, Path planning, Variational Art

Student Number: 2007-30194

Contents

Abstract	i
List of Tables	v
List of Figures	vi
Chapter 1 Introduction	1
1.1 Overview	1
1.2 Configuration of the thesis	7
Chapter 2 Path Planning of a Mobile Robot	9
2.1 Global path planning	9
2.2 Conversion into topology optimization formulation	12
2.2.1 Analogy	12
2.2.2 Heat transfer problem for a path planning	15
2.2.3 Objective function	17
2.2.4 Representation of a map	19
2.2.5 Topology optimization formulation	23
2.3 Indoor global path planning	27
2.3.1 Fundamental examples	28
2.3.2 Path planning avoiding obstacles	30
2.3.3 Continuous curvature path planning	33
2.3.4 Obstacle free path planning of a square robot	43
2.4 Outdoor global path planning	52

2.4.1	Strategy for a mobility representation.....	52
2.4.2	Path planning in a simulated real terrain.....	56
2.4.3	Path planning in a natural terrain represented by DEM.....	60
2.5	Computation cost	66
2.6	Summary	70
Chapter 3 Variational Art.....		72
3.1	Hypothetical analogy	72
3.2	Variational art algorithm	76
3.3	Parameters affecting image output.....	84
3.3.1	Coloring technique.....	84
3.3.2	The effects of parameter group \mathbf{P}_B	87
3.3.3	The effects of parameter group \mathbf{P}_C	93
3.4	Summary	95
Chapter 4 Conclusions		96
Bibliography.....		100
Appendix A Topology Optimization Formulation		110
Appendix B Exhibition and Artworks.....		113
Abstract (Korean).....		136
감사의 글		138

List of Tables

Table 2.1	Comparison of the path planning and heat path design	13
Table 2.2	Nominal values of parameters used in the thesis	27
Table 2.3	Penalty exponent used in each case of Fig. 2.10	30
Table 3.1	Parameters used in the variational art algorithm	82

List of Figures

Figure 2.1	Global path planning	10
Figure 2.2	Analogy of (a) a path planning and (b) topology optimization ..	12
Figure 2.3	Schematics of (a) a configuration space and (b) design domain	14
Figure 2.4	Optimal heat path design problem to substitute the global path planning of a mobile robot.....	16
Figure 2.5	Conductive hat transfer in (a) the one-dimensional problem and (b) two-dimensional problem	18
Figure 2.6	Implicit meaning of the objective function Ψ : the alternative choice to plan a path with minimal length.....	19
Figure 2.7	Flow chart of the path planning algorithm based on topology optimizatin methd	26
Figure 2.8	Fundamental example for a path planning.....	28
Figure 2.9	Results of problem of Fig. 2.8: (a) optimal path, (b) temperature distributions, and (c) sensitivities	28
Figure 2.10	Improved paths by using continuation method. Each exponent penalties are ginven in Table 2.3.....	29
Figure 2.11	Paths generated in workspace (a) where a path exists and (b) where a path is not exist.....	31
Figure 2.12	Work space with scattered polygonal obstacles.....	32
Figure 2.13	Optimal path of the problem of Fig. 2.12	32
Figure 2.14	Iteration histories of a result of Fig. 2.13.....	33
Figure 2.15	Interpretation of symmetric clothoid blending	34
Figure 2.16	Determining of the triplete to be used for symmetric clothoid blending and the interpolated clothoid curve.....	35
Figure 2.17	Triplet of path elements	36
Figure 2.18	The kinds of arrangement of the triplet of path elements:	

	(a) $g > (\sqrt{5}/2)l_e$, (b) $g > l_e$, (c) $g > \sqrt{2}l_e$, and (d) $g > l_e$	36
Figure 2.19	Analysis and interpolation of discretized path elements by using symmetric clothoid blending	38
Figure 2.20	Numerical example: (a) path represented in design domain and (b) its graphical representatin	39
Figure 2.21	Clothoid curve interpolating the path of Fig. 2.22(b): (a) the enlarged part of Fig. 2.21(b) and (b) final smoothing path.....	40
Figure 2.22	Curvature of the path of Fig. 2.23(b): (a) maximum curvature spot and (b) variations of curvature of whole path	41
Figure 2.23	Paths with different control distance g : (a) interpolated path with $g = 1.15$ and (b) the curvature of it, and (c) interpolated path with $g = 1.20$ and (d) the curvatures of it	42
Figure 2.24	Moving square robot avoiding a rectangle obstacle	43
Figure 2.25	Configuration space generated by twisting obstacle.....	44
Figure 2.26	Workspace for the rectangle robot's path planning.....	44
Figure 2.27	Optimal planned path without considering the size and orientation of a robot	45
Figure 2.28	Schematics of a physical pose of a square robot at a given configuration.....	45
Figure 2.29	Feasibility checking: (a) physical poses of a robot on the path and (b) new configuration space.....	46
Figure 2.30	Path planning on a new workspace of Fig. 2.29(b): (a) re-planned path and (b) physical poses of a robot on the path.....	47
Figure 2.31	Workspace with complex obstacles	48
Figure 2.32	The first obstacle-free path	48
Figure 2.33	workspace after 16 times of feasibility checking.....	49
Figure 2.34	The final optimal path designed in workspace of Fig. 2.33.....	49
Figure 2.35	Physical poses of a robot on the final path of Fig. 2.34.....	50

Figure 2.36	Flowchart of the process of feasibility determination	51
Figure 2.37	Surface $g(x, y)$ simulating a real terrain	52
Figure 2.38	Relations between the thermal conductivity and the slope of the surface: (a) top view of the surface of Fig. 2.37 and (b) changes in topography of the cross section cut along $B_1 - B_2$	54
Figure 2.39	Simulated surface of a natural terrain	56
Figure 2.40	The thermal conductivities by Eq. (50): (a) k_x and (b) k_y	57
Figure 2.41	Optimal path planned on the workspace of Fig. 2.39	58
Figure 2.42	Simple paths for comparison with the optimal path of Fig. 2.41: (a) straight line route (Nominal 1), and (b) circular bypass route (Nominal 2).....	58
Figure 2.43	Variations of elevation $g(\mathbf{P}_i)$ along each path.....	59
Figure 2.44	The cumulative distance traveled over the surface	60
Figure 2.45	Natural terrain presented by DEM: (a) 3D view and (b) contour map	61
Figure 2.46	Distributions of the thermal conductivity: (a) top view of the terrain, (b) x-directional thermal conductivity and (c) y-directional thermal conductivity	61
Figure 2.47	Optimal paths planned in real terrain represented by DEM	62
Figure 2.48	Example problem with the maximum slope constraints: (a) DEM of workspace and (b) its elevation contour map	63
Figure 2.49	Distributions of the thermal conductivity and optimal path: (a) x-directional thermal conductivities, (b) y-directional thermal conductivities, and (c) optimal paths	64
Figure 2.50	Paths represented in three dimensional space	64
Figure 2.51	Variations of each path: (a) the elevation and (b) tangent value of a slope angles along each path.....	65

Figure 2.52	Computation process of a path planning based on topology optimization	67
Figure 2.53	Computation cost of each computation process	68
Figure 2.54	Computation cost with different number of CPU	69
Figure 3.1	Hypothetical analogy between (a) brush strokes in painting and (b) the topology optimization problem to find an efficient heat dissipating path on a two-dimensional heat-conducting plate	73
Figure 3.2	Simultaneous generation of multiple heat paths when multiple heat sources and sinks are used. (a) An example of distributed heat sinks and sources and (b) multiple optimized paths.....	74
Figure 3.3	Virtual system of heat transfer that is used to develop the variational art algorithm	76
Figure 3.4	Discretized model of the virtual physical system	78
Figure 3.5	Flow chart of the proposed variational art algorithm	81
Figure 3.6	Schematic description of the creation of a multi-color image for $n_L = 2$. The final image is obtained by a color mixing technique (j : iteration number).....	83
Figure 3.7	The color variation in an element according to Eq. (3.19) (the color triplet C_e^j is arbitrarily chosen as $[200,150,70]$).....	85
Figure 3.8	Superposed images based on the proposed color mixing rule in Eq. (3.20) (j : iteration number).....	86
Figure 3.9	The effect of the source-sink distance on generated image. The canvas region is discretized by 400×400 elements. ($M = 0.3$, $Q^* = 1$, $h^* = 1$, $p = 3$, $n_{iter} = 20$) The height and width of every element are unity (units are ignored). (a) Distance = $2\sqrt{2}$, (b) Distance = $100\sqrt{2}$, (c) Distance = $300\sqrt{2}$	88
Figure 3.10	The effects of varying the number of heat sinks (ending points)	

	for a single heat source (starting point) ($M = 0.3$, $Q^* = 1$, $h^* = 1$, $p = 3$, $n_{iter} = 20$) (a) $N^E = 2$, (b) $N^E = 4$, (c) $N^E = 10$	89
Figure 3.11	The effects of varying the number of heat sources (starting points) for a single heat sink (ending point) ($M = 0.3$, $Q^* = 1$, $h^* = 1$, $p = 3$, $n_{iter} = 20$) (a) $N^S = 2$, (b) $N^S = 4$, (c) $N^S = 10$	89
Figure 3.12	Results of numerical experiments with varying ratios of the magnitudes of two sinks for a single source of fixed magnitude. ($M = 0.3$, $Q^* = 1$, $p = 3$, $n_{iter} = 20$) (a) $h_1^* : h_2^* = 1:1$, (b) $h_1^* : h_2^* = 3:1$, (c) $h_1^* : h_2^* = 5:1$	91
Figure 3.13	Results of numerical experiments with varying ratios of the magnitudes of two sources for a single sink of fixed magnitude. ($M = 0.3$, $h^* = 1$, $p = 3$, $n_{iter} = 20$) (a) $Q_1^* : Q_2^* = 1:1$, (b) $Q_1^* : Q_2^* = 3:1$, (c) $Q_1^* : Q_2^* = 5:1$	91
Figure 3.14	Experiments with different numbers of sinks and sources. ($M = 0.3$, $Q^* = 1$, $h^* = 1$, $p = 3$, $n_{iter} = 20$) (a) $(N^S, N^E) = (25, 25)$, (b) $(N^S, N^E) = (100, 100)$, (c) $(N^S, N^E) = (200, 200)$ (the sink and source locations are randomly assigned).....	92
Figure 3.15	Images obtained with varying maximum iteration numbers. ($M = 0.3$, $Q^* = 1$, $h^* = 1$, $p = 3$).....	93
Figure 3.16	The effects of the mass constraint ratio on the obtained images. ($Q^* = 1$, $h^* = 1$, $p = 3$, $n_{iter} = 20$).....	93
Figure 3.17	The effects of the penalty exponent on the obtained images.	

($M = 0.3$, $Q^* = 1$, $h^* = 1$, $n_{iter} = 20$) (a) $p = 1$, (b) $p = 3$ 94

Figure A.1	Flow chart of topology optimization of thermal structure	111
Figure B.1	Exhibition title and description.....	114
Figure B.2	Media art displayed in exhibition	114
Figure B.3	Body series No. 3, Project 33, 2011.....	115
Figure B.4	Body series No. 12, Project 33, 2011.....	116
Figure B.5	Body series No. 28, Project 33, 2011.....	117
Figure B.6	Drawing series No. 2, Project 33, 2011	118
Figure B.7	Drawing series No. 5, Project 33, 2011	119
Figure B.8	Drawing series No. 9, Project 33, 2011	120
Figure B.9	Figure series No. 3, Project 33, 2011	121
Figure B.10	Figure series No. 8, Project 33, 2011.....	122
Figure B.11	Figure series No 17, Project 33, 2011.....	123
Figure B.12	Skeleton series No. 7, Project 33, 2011	124
Figure B.13	Skeleton series No. 65, Project 33, 2011	125
Figure B.14	Skeleton series No. 72, Project 33, 2011	126
Figure B.15	Manikin series No. 4, Project 33, 2011.....	127
Figure B.16	Manikin series No. 8, Project 33, 2011.....	128
Figure B.17	Manikin series No. 10, Project 33, 2011.....	129
Figure B.18	Abstract series No. 4, Project 33, 2011.....	130
Figure B.19	Abstract series No. 12, Project 33, 2011.....	131
Figure B.20	Abstract series No. 25, Project 33, 2011.....	132
Figure B.21	Figure series II No. 3, Project 33, 2011	133
Figure B.22	Figure series II No. 11, Project 33, 2011	134
Figure B.23	Figure series II No. 24, Project 33, 2011	135

Chapter 1

Introduction

1.1 Overview

Topology optimization is one of the structural optimization techniques. The purpose of the method is an optimal design of structures and mechanical component. Since topology optimization technique based on the homogenization method has been proposed in 1988 by Bendsøe and Kikuchi [1], the method has widened its scope of applications. Today, as successfully applied to the design of a leading edge rib of A380 [2], topology optimization is technically very mature in structural design [3,4,5,6]. In addition, structural topology optimization technique related to the various physics such as heat transfer [7,8,9,10], fluidic flow [11,12,13], electromagnetic [14,15,16], noise and vibration [17,18,19] etc has been much studied. In addition to these traditional areas of mechanics, topology optimization method is applied not only to a link design [20] and a new material design for energy harvesting [21] but also applied even to a prediction of protein folding structure [22,23]. In this thesis, topology optimization technique will be applied to an engineering problem which has not been tried to solve by topology optimization so far. That is a robot path planning problem and which is the first topic of the thesis [24]. Furthermore, the convergence research of engineering technique and aesthetic visual design will be attempted. That is

the variational art algorithm¹ and which is the second topic of the thesis.

The path planning problem is one of the most fundamental problems in robotics and has received considerable attention in the literature [25, 26, 27]. In its simplest formulation, one seeks a path in configuration space connecting a pair of given points while avoiding any obstacles. Perhaps the most widely used methods today are those classified as probabilistic roadmap methods (PRM). An overview and survey can be seen in the recent literatures of Svestka and Overmars [28] and Choset et al. [25]. Typically the configuration space is high dimensional and often cluttered due to the presence of obstacles. PRM methods take random samples from the feasible region of the configuration space, and attempt to find a feasible path connecting these points, typically using graph representations. The PRM methodology has been combined with various optimal control and potential field-based methods for improving performance [25,29,30]. Another set of widely used methods are based on artificial potential fields [31]. In this method, the goal point and obstacles are defined as attractive and repulsive potentials, respectively. The direction of steepest decent, obtained by differentiating the total sum of the potentials, is then chosen as the direction of motion. Because of the simplicity of the algorithm, it is easy to understand mathematically and the cost of calculation is small. The main drawback is the occurrence of the so-called deadlock, a kind of local minima. Various approaches have been proposed to avoid deadlock and other phenomena. In particular, Koditchek and Rimon [32] proposed the so-called navigation functions. Motivated in part by a desire to more naturally overcome the deadlock problem, a variety of potential field-

¹ Korean Patent Registered (Jan., 2011), US Patent Pending

based methods inspired by physics and mechanics have recently been suggested. Kim and Khosla [33] suggested a method using streams of particles within the potential flow, while Masoud et al. [34] proposed a biharmonic potential approach using an analogy with a mechanical stress field. Singh et al. [35] used a magnetic analogy, while an analogy with fluid dynamics was made by Keymeulen and Decuyper [36]. Louste and Liegeois [37] also suggested a method using a potential viscous fluid analogy; in their approach, they provide both a minimum energy path as well as a shortest path by varying the viscosity in the energy function. The unsteady diffusion equations were also used by Schmidt and Azarm [38]. In this paper, we suggest an alternative approach to navigate the shortest robot path.

The main idea is to set up the path planning problem as a topology optimization problem. Although topology optimization [1] has been widely used in several disciplines, there has been no attempt to use it for robot path planning problems. The use of the topology optimization in path planning has some advantages over existing methods, as shall be listed below; the proposed approach possibly offers a different perspective on the problem. The method suggested in this thesis was started from this observation and has effectively addressed a variety of path planning problems. For example, we have addressed the original problem that plans the path avoiding obstacles, smoothing path problem that plans a continuous curvature path for a car-like robot, and long range routing problem [39, 40] that plans the path in huge real terrain.

The results are very encouraging. Compared with conventional approaches, the proposed method has various advantages. Among them, the followings are

representatives. The first is that it is not affected by the complexities of the map. For example, the computation time is necessary affected only the size of the map. The complexities of a map such as the number, shape, and density of obstacles never effect. The second is that the map building and re-building is very easy. Our method can use the DEM (digital elevation map) directly. And also, different from the conventional graph map representation, new obstacles can be easily added to the previous map without re-building of an entire map, which is very hard work in general. The third is a good quality of a path. Because that topology optimization find the optimal path using optimization technique, it is easy to implement finding some specific path. Although, in this thesis, only shortest path finding problems are solved by using the minimization of thermal compliance, the possibility to find various optimal paths by formulating the suitable objective functions is abundant. And also, the resultant path obtained from the proposed method is constructed by the consecutive of finite elements. In other words, compared to the graphical paths being composed with the vertices and edges, the information of the path is abundant and exact. This quality of the path is very useful to the smoothing technique interpolating the path as smooth curve, which is executed secondly after obtaining the path.

On the other hand, proposed method has disadvantages also. The main disadvantage is the high cost of computation time. As mentioned earlier, compared to conventional graph search algorithms [25], the computation time is long. This is not avoidable property originated from the FEM (finite element method) used in the proposed method. However, although it is hard to make better than the graph search algorithms, there is a change to improve.

For example, the parallel processing widely used in various image filtering can be applied to it. And it has been demonstrated already in this thesis that the matrix assembly time can be reduced by parallel processing [41].

The variational art algorithm is the convergence research of engineering and art. Its motivation is originated from the study applying topology optimization into the path planning problem. Phenomenally, the path is a line. In other words, path planning is to draw the line. And drawing a line is fundamentals of image creations. Moreover, by appropriately adjusting various parameters, novel images can be created. Practically, the various artistic images can be created.

Since computational algorithms for art or aesthetic design were suggested in the early 1960s [42, 43], there has been a growing interest in utilizing them for non-engineering or scientific fields. For instance, fractal images [44] that are generated by mathematical equations have received attention as they provide unique aesthetic values. Images generated by computer algorithms or those representing some physical phenomena have influenced artists and designers in various ways. Recently, attempts to use evolutionary algorithms [45, 46, 47] have also been made for image generation. Besides evolutionary algorithms, several other approaches have been developed, such as the parametric method [48] for decorative Islamic pattern generation and an algorithm to simulate fungal hyphae growth [49]. Other researchers have attempted to generate or create images by mimicking various phenomena observed in nature [50, 51]. In the literature described above, images are mostly generated by simulating biological or physical phenomena. Unlike the

aforementioned approaches to simulating physical phenomena, we are proposing a new image generation method; a method to solve "physics-based optimization" problems. More specifically, topology optimization problems to find efficient heat dissipating structures in a two-dimensional plate are solved for image creation. An underlying thought in using an optimization problem involving a physical principle is that optimization could produce interesting, yet artistically acceptable images.

As mentioned above, the variational art algorithm is the convergence research. So, the value of it should be recognized from not only engineering but also art. Because it is not suitable to recognize the artistic values in this thesis, it is not mentioned in this thesis. However, it should be mentioned that the variational art had won at the competition of 2011's Art Space, Seogyo and the artworks had been exhibited at Art Space, Seogyo from 11 to 19, November, 2011. Some examples are added in Appendix B. From the point of engineering view, the properties of the parameters affecting the image are suggested and studied in the text. And also some different formulation of color mixing techniques is suggested. Compared to the various image processing tools used conventionally, the variational art algorithm has originality that images are created in by the mathematical optimization process and physical simulation of heat transfer. From this reason, the user (artist) cannot control the resultant image perfectly. From some point of view, this is a disadvantage. However, this study is just the beginning and the controllability of the resultant artwork will be improved in the near future.

1.2 Thesis configuration

The work suggested in this thesis has two main topics. For the first topic, the global path planning algorithm of a mobile robot by using equivalent topology optimization of a conductive heat transfer structure is dealt with in Chapter 2. And then, the computer-aided aesthetic design algorithm referred as a variational art algorithm will be presented in Chapter 3. The fundamentals of topology optimization of heat transfer are given at Appendix A. In addition, Appendix B shows some artistic works created by variational art algorithm.

Chapter 2 has studied the global path planning of a mobile robot. The path planning problem is one of the most fundamental problems in robotics and has received considerable attention. The problem can be summarized as finding a path connecting a pair of given points while avoiding obstacles. To solve this problem, the path planning problem will be formulated as a topology optimization problem that minimizes thermal compliance. Because the classical topology optimization formulation for a thermal structure is inappropriate for a path planning, we will suggest modified topology optimization formulation. The practicality of the suggested method is validated through various numerical examples.

Chapter 3 deals with variational art algorithm. The “variational art” is newly named to indicate the computer-aided aesthetic design. As a kind of interdisciplinary conversion research, this is a research of the non-traditional application of topology optimization technique. To realize aesthetic design by

the optimization method, we propose to view brushing activities in painting as being equivalent to finding an optimal path connecting heat sinks and sources on a two-dimensional heat-transferring plate under a mass constraint. There are several parameters to be controlled to produce a number of different images. The detailed algorithm for the proposed computer-aided aesthetic design is presented and the effects of various parameters on the obtained images will be studied. Some representative artworks obtained by the proposed approach are also presented.

Chapter 2

Path Planning of a Mobile Robot

2.1 Global path planning

The ultimate goal of robotics is to complement and replace the human operating by the own planning and judgment of an artificial intelligence. Thus, the development of an efficient path planning algorithm of a robot is a key problem in robotics. Human can determine their own action by considering the situation of a surrounding terrain and obstacles immediately and accomplish their own objectives. But, unlike humans, robots do not have a reasonable ability to do this comprehensively by assessing their own situation. The robot path planning algorithm is to confer the reasonable ability with which a robot by itself can perform a given task to a robot. In engineering the robot path planning is defined more precisely as follows:

“The prototypical task is to find a path for a robot, whether it is a robot arm, a mobile robot, or a magically free-flying piano, from one configuration to another while avoiding obstacles” [25]

A basic concept of the path planning problem is defined simply as mentioned above. But, according to a type and intended use of a robot, various types of path planning problems are defined. For example, a robot path planning can be categorized as motion planning, local navigation, global path planning, and

trajectory planning. More details about each category can be found in the technical memorandum of Giesbrecht. [52] In this thesis, I am focused on the global path planning problem. Global path planning problem, as shown in Figure 2.1, is to plan the trajectory for a robot to move from a given starting position to the final target position. According to Giesbrecht, global path planning is defined as follows:

“Planning which encompasses all of the robot’s acquired knowledge to reach a goal, not just the current sensed world. It is slower, more deliberative, and attempts to plan into the future. There is generally no requirement for it to run in real time, but instead is usually run as a planning phase before the robot begins its journey.” [52]

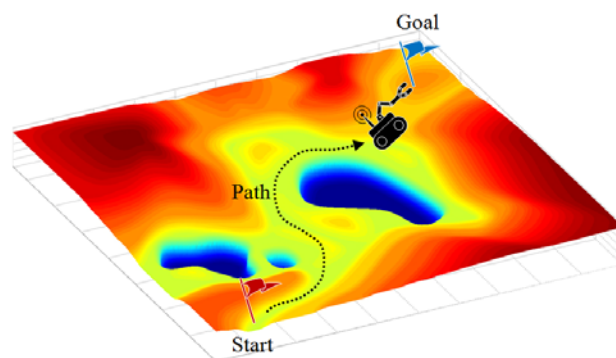


Figure 2.1 Global path planning

To solve a global path planning problem of a mobile robot, the following objectives will be met.

Obstacle avoidance path

Obstacles are the conditions to block the movement of a robot. Thus, a robot on the planned path must not pass through these obstacles. And also a robot should not be in contacts with these obstacles.

Robot size/shape

In the case of outdoor robot path planning, the robot can be thought of as points. However, in the case of indoor path planning of a robot working in the factory, office, home-like environment, the size and shape of a robot is a very important factor.

Goal of the path

The robot's path must achieve a particular purpose. In other words, according to a robot's work various objectives such as the minimization of travel distance, travel time, and energy consumption will be demanded. In this research, only the minimization of travel distance is covered.

Exact Notification

In some cases, it may be impossible that the path of a robot is found in a given environment. In this case, the path planning algorithm will have to tell that there is no path.

2.2 Conversion into Topology Optimization Formulation

2.2.1 Analogy

The problem to design an efficient heat path that transfers heat energy from a heat source to sink is one of the general applications of topology optimization. The topology optimization process of thermal structure is already described in Appendix A. As shown in Fig. 2.2, the optimal heat path design and the path planning problem are very similar in problem configuration.

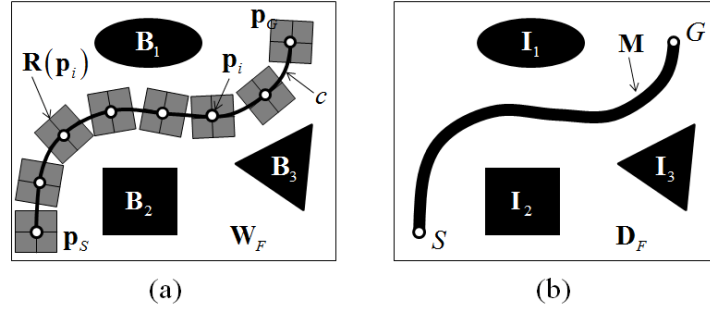


Figure 2.2 Analogy of (a) a path planning and (b) topology optimization

Figure 2.2(a) shows a global path planning problem. The whole space W is a workspace. The space B_i ($i=1,2,3$), which are occupied by obstacles, are called as obstacle spaces. If B_i are randomly distributed in W , the entire obstacle space W_B is defined as the union of all B_i . Thus, the free space W_F in which a robot can move freely becomes the difference set of W and W_B . It can be summarized as follows:

$$W_B = \bigcup_i B_i \quad (2.1)$$

$$\mathbf{W}_F = \mathbf{W} \setminus \mathbf{W}_B \quad (2.2)$$

The path of the mobile robot is defined as a continuous curve c in \mathbf{W}_F , which connects a starting point \mathbf{p}_S and a goal point \mathbf{p}_G . On the other hand, Figure 2.2(b) shows topology optimization of conductive heat path design. The conductive heat path will be designed in a given design space, which is symbolized by \mathbf{D} . Design domain includes insulators \mathbf{I}_i ($i=1,2,3$). In this case, the entire union of \mathbf{I}_i is defined as non-design domain \mathbf{D}_I and the difference set of \mathbf{D} and \mathbf{D}_I is defined as design domain \mathbf{D}_F . This can be summarized as follows:

$$\mathbf{D}_I = \bigcup_i \mathbf{I}_i \quad (2.3)$$

$$\mathbf{D}_F = \mathbf{D} \setminus \mathbf{D}_I \quad (2.4)$$

In the heat path design problem, a heat path will be obtained as continuous distributions of mass \mathbf{M} , which is connecting a heat source S and sink G . This similarity is summarized in Table. 2.1.

Table 2.1: An analogy between path planning and a heat path design

Global Path Planning		Topology Optimization
Starting Point	↔	Heat Source
Goal Point	↔	Heat Sink
Obstacles	↔	Insulators
Free Workspace	↔	Free Design Domain
Path of a Robot	↔	Heat Path

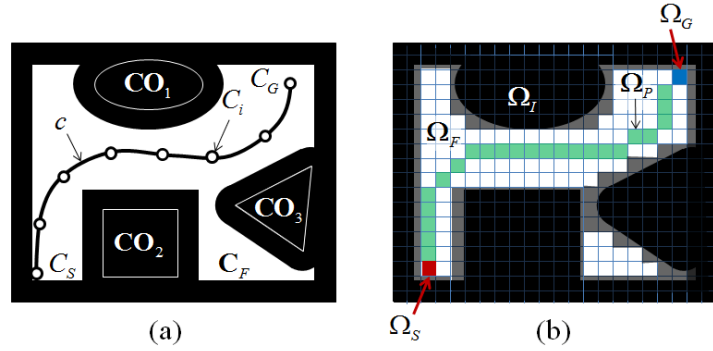


Figure. 2.3 Schematics of (a) a configuration space and (b) design domain

In practical, a path is planned in the configuration space. The configuration space, which will be symbolized as C , is different with a work space. C is the space that composed with the state set of a robot which called as a configurations. For example, one configuration can describe the velocity, direction, size, position, etc. To plan the path, W should be converted to C . Figure 2.3(a) shows C converted from W of Fig. 2.2(a). In this case, the configuration C_i of a robot is defined simply as a position vector P_i of the center of movement of a robot. So, $C_i = P_i$. When a robot located at $P_i (= C_i)$, a physical space occupied by a robot in W is defined as $R(P_i)$. And then, the obstacle configuration CO and free configurations C_F can be defined as follows:

$$CO = \{C_i | R(P_i) \cap W_B \neq \emptyset, C_i = P_i\} \quad (2.5)$$

$$C_F = C \setminus CO \quad (2.6)$$

Global path planning is to find a continuous path trajectory c , which is a set

of consecutive $C_i (i=1, \dots, n)$ connecting starting configuration C_s and goal configuration C_G in C_F . On the other hands, Fig. 2.3(b) shows the discretized design domain of Fig. 2.3(a) and topology optimization process is executed in this discretized domain. So, the configuration obstacles and free configurations are represented by the set of finite elements of which conductivity is almost zero and set of finite elements of which conductivity is non-zero value as follows:

$$\Omega_I = \{\Omega_e | k_e \ll 1\} \quad (2.7)$$

$$\Omega_F = \Omega \setminus \Omega_I \quad (2.8)$$

In Eq. (2.7), e means the number of element and k_e is the thermal conductivity of e^{th} element. At the same time, the path Ω_p is constructed by the set of elements of which density value is one as follows:

$$\Omega_p = \{\Omega_e | \rho_e = 1\} \quad (2.9)$$

where ρ_e is the design variable of e^{th} element. More details are described in Section 2.2.4.

2.2.2 Heat transfer problem for a path planning

Figure 2.4 shows the conduction heat path design problem to replace for the global path planning problem. As can be seen in Fig. 2.4, the problem is defined in two-dimensional plate Ω .

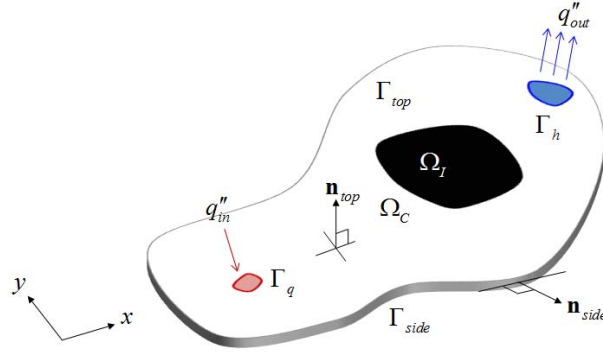


Figure 2.4 Optimal heat path design problem to substitute the global path planning of a mobile robot

Design area Ω is made up of the area for different kinds of thermal conductivity. In Fig. 2.4, Ω is simply divided into two regions; conductor area Ω_C and insulator area Ω_I . There relations are $\Omega = \Omega_C \cup \Omega_I$ and $\emptyset = \Omega_C \cap \Omega_I$. In addition, a heat flux q''_{in} is coming from the surface $\Gamma_q \subset \Gamma_{top}$ and another heat flux q''_{out} is exit at the different surface $\Gamma_h \subset \Gamma_{top}$. The adiabatic boundary conditions are given at all aspect boundaries Γ_{side} . Summarizing the above are as follows:

$$\frac{\partial}{\partial x} \left(k_x \frac{\partial \theta}{\partial x} \right) + \frac{\partial}{\partial y} \left(k_y \frac{\partial \theta}{\partial y} \right) = 0 \quad (2.10)$$

$$q''_{in} = \bar{q} \text{ on } \Gamma_q \quad (2.11)$$

$$q''_{out} = h\theta \text{ on } \Gamma_h \quad (2.12)$$

$$\frac{\partial \theta}{\partial \mathbf{n}_{top}} = 0 \text{ on } \Gamma_{top} / \Gamma_h \quad (2.13)$$

$$\frac{\partial \theta}{\partial \mathbf{n}_{side}} = 0 \text{ on } \Gamma_{side} \quad (2.14)$$

2.2.3 Objective function

In order to set up the topology optimization formulation for the heat transfer problem defined in previous section, an appropriate objective function Ψ has to be selected. In this research, the thermal compliance minimization is selected as an objective function. It means to minimize the dissipation of heat transfer potential capacity Ψ . Ψ is defined as follow: [53, 54]

$$\Psi = \frac{1}{2}k(\nabla T)^2 \quad (2.15)$$

T and k of Eq. (2.15) are the temperature and thermal the conductivity respectively. Physical meaning of Ψ can be considered as the reduction of a heat transfer capability when a substance transfer a heat. Thus, the heat transfer efficiency (η) in a structure of a small Ψ is bigger than that in a structure of a large Ψ . [53] Therefore, the usage of Eq. (2.15) as the objective function eventually means to design the heat path which maximizes η . However, Eq. (2.15) alone is not clear to explain what the heat path maximizing η means in relation to the path planning of a mobile robot. Thus the maximization of η is necessary to explain from a different physical perspective. η is directly related to the thermal resistance (R_t) of the structure. In other words, what η of the structure is large is such that R_t of the structure is small. For more details consider the case of Fig. 2.5.

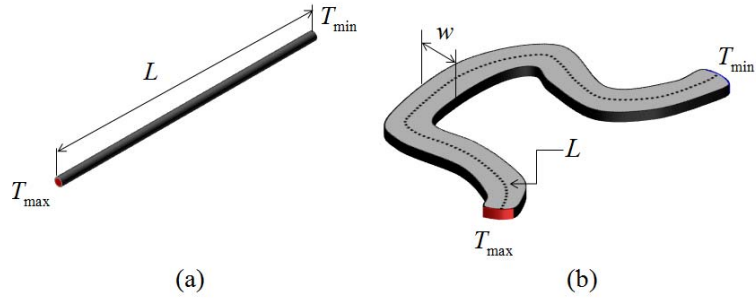


Figure 2.5 Conductive heat transfer in (a) the one-dimensional problem and (b) two-dimensional problem

R_t of the structure in one-dimensional conduction heat transfer of Fig. 2.5(a) is defined as follows: [55]

$$R_{t,cond} \equiv \frac{T_{\max} - T_{\min}}{q} = \frac{L}{kA} \quad (2.16)$$

In Eq. (2.16), T_{\max} and T_{\min} , respectively, mean temperature of two points, and L is the distance between T_{\max} and T_{\min} . And A and k are cross-sectional area and thermal conductivity respectively. In the case of Eq. (2.16), the minimization of $R_{t,cond}$ is same as the minimization of L . Although Eq. (2.16) is derived from one-dimensional problem, with some assumptions, it can be applied into the two-dimensional plate of Fig. 2.5(b). For example, if the width of the structure (w) is constant or much smaller than L , it is reasonable to apply Eq. (2.16) on the two-dimensional case.

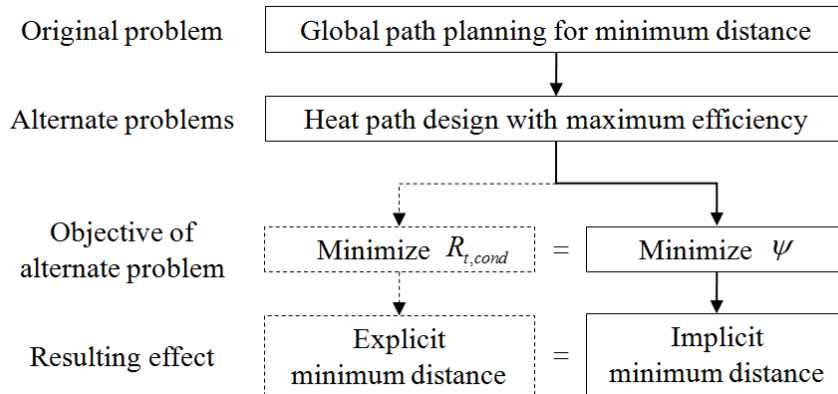


Figure 2.6 Implicit meaning of the objective function Ψ : the alternative choice to plan a path with minimal length

Figure 2.6 shows an overview of the process of setting up the objective function to minimize travel distance of a robot. The shortest path planning problem is same as the heat path design problem maximizing the heat transfer efficiency. To maximize η , we can choose two different objective functions; minimization of Ψ and maximization of $R_{t,cond}$. Equation (2.16) explicitly shows that the maximization of $R_{t,cond}$ can construct the shortest heat path. In fact, Wang and Chirickjian used the maximization of $R_{t,cond}$ as the objective function in their research. [56] However, because we will find the robot path based on the topology optimization method, the minimization of Ψ is chosen as the objective function in this research.

2.2.4 Representation of a map

To plan the path of a mobile robot, the process of converting the physical

workspace (\mathbf{W}) in the configuration space (\mathbf{C}) is already explained in section 2.2.1. And, to apply topology optimization method into path planning problem, it was mentioned already that \mathbf{C} should be converted into the design space ($\mathbf{\Omega}$). In topology optimization, Finite Element Method is used as an analysis tool. So, $\mathbf{\Omega}$ consists of the regular square mesh so that the FEM can be applied. Figure 2.3(b) shows $\mathbf{\Omega}$ represented by finite elements. All the element partially containing \mathbf{CO} is defined as an insulator element and the union of these elements is defined as non design domain $\mathbf{\Omega}_I$. And the union of all other elements except $\mathbf{\Omega}_I$ is defined as a design domain $\mathbf{\Omega}_F$. On the other hand, each finite element which includes \mathbf{C}_S and \mathbf{C}_G is, respectively, defined as the heat source element $\mathbf{\Omega}_S$ and heat sink element $\mathbf{\Omega}_G$. $\mathbf{\Omega}_S$, $\mathbf{\Omega}_G$, $\mathbf{\Omega}_I$, and $\mathbf{\Omega}_F$ are formulated as follows.

Source element ($\mathbf{\Omega}_S$)

The heat source in $\mathbf{\Omega}$ is represented by $\mathbf{\Omega}_S$. The quantity of incoming heat flux (q''_{in}) determine the boundary condition of $\mathbf{\Omega}_S$. Thus it is included in the load term of Eq. (A.3) (See, Appendix A). At the same time it makes up the element load vector at the level of element matrix equation. In this case, \mathbf{f}_{e_s} is presented and computed as follows:

$$\mathbf{f}_{e_s} = \left[\phi_1^{e_s} \quad \phi_2^{e_s} \quad \phi_3^{e_s} \quad \phi_4^{e_s} \right]^T \quad (2.17)$$

$$\phi_i^{e_s} = \int_{\Gamma} N_i \bar{q} d\Gamma \quad (2.18)$$

In Eq. (2.18), \bar{q} is a given value of heat flux.

Sink element (Ω_G)

The heat sink in Ω is represented by Ω_G . The heat loss is generated as much as q''_{out} at e_G . Thus, q''_{out} also determine the boundary condition of e_G . However, unlike q''_{in} , q''_{out} can be calculated as a part of the stiffness matrix of Eq. (A.3) (See, Appendix A). \mathbf{k}_{e_G} of e_G is evaluated as the sum of $\mathbf{k}_{e_G}^k$ and $\mathbf{k}_{e_G}^h$ as follow:

$$\mathbf{k}_{e_G} = \mathbf{k}_{e_G}^k + \mathbf{k}_{e_G}^h \quad (2.19)$$

In Eq. (2.19), by the condition $q''_{out} = h\theta$ of Eq. (2.12), $\mathbf{k}_{e_G}^h$ is presented and computed as follows:

$$\mathbf{k}_{e_G}^h = \begin{bmatrix} [\mathbf{K}^h]_{11}^{e_G} & [\mathbf{K}^h]_{12}^{e_G} & [\mathbf{K}^h]_{13}^{e_G} & [\mathbf{K}^h]_{14}^{e_G} \\ [\mathbf{K}^h]_{21}^{e_G} & [\mathbf{K}^h]_{22}^{e_G} & [\mathbf{K}^h]_{23}^{e_G} & [\mathbf{K}^h]_{24}^{e_G} \\ [\mathbf{K}^h]_{31}^{e_G} & [\mathbf{K}^h]_{32}^{e_G} & [\mathbf{K}^h]_{33}^{e_G} & [\mathbf{K}^h]_{34}^{e_G} \\ [\mathbf{K}^h]_{41}^{e_G} & [\mathbf{K}^h]_{42}^{e_G} & [\mathbf{K}^h]_{43}^{e_G} & [\mathbf{K}^h]_{44}^{e_G} \end{bmatrix} \quad (2.20)$$

$$[\mathbf{K}^h]_{ij}^{e_G} = h \int_{e_G} N_i N_j de_G \quad (2.21)$$

h of Eq. (2.21) is the convection heat transfer coefficient. On the other hand,

$\mathbf{k}_{e_G}^k$ of Eq. (2.19) will be explained next section.

Insulator elements (Ω_I) / Conductor elements (Ω_F)

Ω_I can not make up a heat path, so thus it serves as an obstacle of a robot path planning problem. The remaining elements of Ω except Ω_I are defined as Ω_F that can potentially make up a heat path. Ω_I and Ω_F are identified by using a different thermal conductivity. The thermal conductivity of each of them is defined as follows:

$$k_x^e = k_y^e = \varepsilon \quad (\varepsilon \ll 1, \Omega_e \in \Omega_I) \quad (2.22)$$

$$k_x^e = k_x^0 ; k_y^e = k_y^0 \quad (\Omega_e \in \Omega_F) \quad (2.23)$$

In Eq. (2.22), ε is given such as a very small value but gives a nonzero value to prevent the stiffness matrix be singular. k_x^0 and k_y^0 of Eq. (2.23) are the thermal conductivities along the x-axis and y-axis respectively. They are given nominal values. In this research, ε is determined as $\varepsilon = 10^{-3}$. The thermal conductivity defined in Eq. (2.22) and Eq. (2.23) will be included on \mathbf{k}_e^k . \mathbf{k}_e^k is calculated as follows:

$$\mathbf{k}_e^k = \begin{bmatrix} [\mathbf{K}^k]_{11}^e & [\mathbf{K}^k]_{12}^e & [\mathbf{K}^k]_{13}^e & [\mathbf{K}^k]_{14}^e \\ [\mathbf{K}^k]_{21}^e & [\mathbf{K}^k]_{22}^e & [\mathbf{K}^k]_{23}^e & [\mathbf{K}^k]_{24}^e \\ [\mathbf{K}^k]_{31}^e & [\mathbf{K}^k]_{32}^e & [\mathbf{K}^k]_{33}^e & [\mathbf{K}^k]_{34}^e \\ [\mathbf{K}^k]_{41}^e & [\mathbf{K}^k]_{42}^e & [\mathbf{K}^k]_{43}^e & [\mathbf{K}^k]_{44}^e \end{bmatrix} \quad (2.24)$$

$$[\mathbf{K}^k]_{ij}^e = k_x^e \int_e \frac{N_i}{\partial x} \frac{N_j}{\partial x} de + k_y^e \int_e \frac{N_i}{\partial y} \frac{N_j}{\partial y} de \quad (2.25)$$

2.2.5 Topology optimization formulation

In Appendix A, general formulation of topology optimization for a thermal structure design was explained. And also the elementary process of setting up heat path design for a path planning has been described in previous section. However, the typical formulation of topology optimization described in Eq. (A.3), Eq. (A.4) and Eq. (A.5) is not suitable enough to solve a path planning problem directly. Although it is confirmed in Section 2.2.3 that the thermal compliance of Eq. (A.3) can be applied directly as the objective function of the shortest path planning problem, the common mass constraint of Eq. (A.4) is not appropriate as well as unnecessary in path planning problem. To solve this problem, this paper uses the following modified formulation:

$$\underset{(\gamma_1, \gamma_2, \gamma_3, \dots, \gamma_N)}{\text{minimize}} \quad \Pi = \boldsymbol{\theta}^T \mathbf{K} \boldsymbol{\theta} = \sum_{e=1}^N (\boldsymbol{\theta}^e)^T \mathbf{k}_e (\boldsymbol{\theta}^e) \quad (2.26)$$

$$\sum_{e=1}^{N_e} \gamma_e v_e - \max(\mathfrak{N}(n), M_{\min}) \leq 0 \quad (2.27)$$

$$\mathfrak{N}(n) = \sum_{e=1}^N v_e / n^2 \quad (2.28)$$

$$M_{\min} = |\mathbf{P}_G - \mathbf{P}_S| v_e / \sum_{e=1}^N v_e \quad (2.29)$$

$$0 < \varepsilon \leq \gamma_e \leq 1 \quad (e = 1, 2, \dots, N; \varepsilon = \text{very small value}) \quad (2.30)$$

Variables of the above equations are defined as follows:

N : Total number of finite elements

v_e : The volume of an individual finite element

$\aleph(n)$: The function of mass constraint

M_{\min} : The allowable minimum mass

n : Number of iteration

\mathbf{P}_G : Position vector of heat sink point

\mathbf{P}_S : Position vector of heat source point

Compared with Eq. (A.3), Eq. (A.4) and (A.5) of Appendix A, you can see that Eq. (A.4) has been switched by Eq. (2.27), Eq. (2.28) and Eq. (2.29). Equation (2.27) implies that the allowed mass of the constraint is gradually reduced to M_{\min} from 1 as iteration progresses. $\aleph(n)$ of each iteration step (n) and M_{\min} is determined by Eq. (2.28) and Eq. (2.29) respectively. Equation (2.29) says that the distance from \mathbf{P}_S to \mathbf{P}_G is used as the allowable minimum mass based on the reasonable assumption that the heat transfer path can not be shorter than the straight-line distance. In fact, because of avoiding the adiabatic sections, most of the heat path will be longer than $|\mathbf{P}_G - \mathbf{P}_S|$. Therefore, all design variables making up the heat path can not converge to a value of 1. This imperfection causes problem on evaluating the convergence criterion. So, in this research, the maximum number of iteration is used to evaluate the additional stopping condition. On the other hand, the approximation of the thermal conductivity of Eq. (A.1) is defined as following by applying the continuation method: [57]

$$k_e = k_0 \gamma_e^{p(n)} \quad (2.31)$$

$p(n)$ of Eq. (2.31) is penalty exponent function and is calculated follow:

$$p(n) = \begin{cases} 1 & \text{when } n < n^* \\ \min(1 + sn, p_{\max}) & \text{when } n \geq n^* \end{cases} \quad (2.32)$$

n^* is a pre-given value and s is a increment for iteration step. p_{\max} is a maximum penalty exponent. In this paper, $s = 0.2$ and $p_{\max} = 3$ are used.

The filtering method of Eq. (A.7) in Appendix A is designed to prevent the checker board problem in the structural design. The filtering method is still available for the path planning problem because the checker board problems are generated in some cases. However, to obtain a clearer path, the filtering method is used restrictively; after a certain number of iteration (n^{**}), the filtering method is not applied any more. The entire optimization process described until now is summarized in the flow chart of Fig. 2.9. In the next section, various numerical examples will be examined to demonstrate the effectiveness of the proposed method.

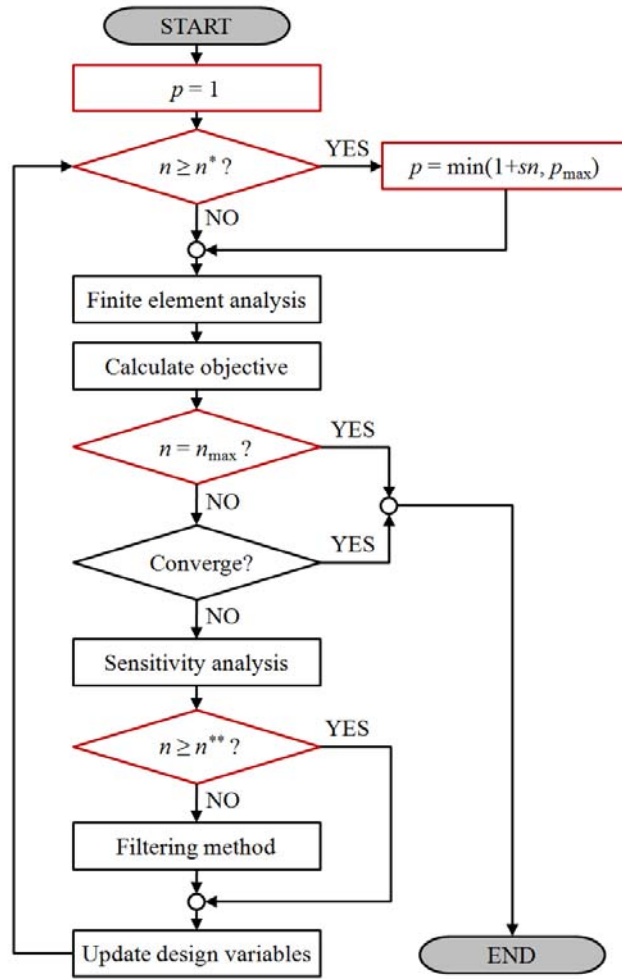


Figure 2.7 Flow chart of the path planning algorithm based on topology optimization method

2.3 Indoor global path planning

In this section, the global path planning problems will be addressed by topology optimization algorithm described in previous section. Although the path planning process is based on the heat transfer phenomenon, the heat transfer analysis exactly corresponding to the physical phenomenon is not necessary to the path planning. Therefore, each initial conditions and parameters were set to a value that is relatively simple and ideal. Table 2.2 shows the values of parameters used in this thesis.

Table 2.2: The values of parameters used in this thesis

Nominal thermal conductivity in x direction ($k_x^0 = 1$)
Nominal thermal conductivity in y direction ($k_y^0 = 1$)
Convection heat transfer coefficient ($h = 1$)
Heat flux inlet at the heat source ($\bar{q} = 1$)
Value of each finite element ($v_e = 1$)
Edge length of finite element ($l_e = 1$)
Maximum number of iteration ($n_{\max} = 40$)
Number of iteration for change of penalty exponent ($n^* = 10$)
Step of increase of penalty exponent ($s = 0.1$)

2.3.1 Fundamental examples

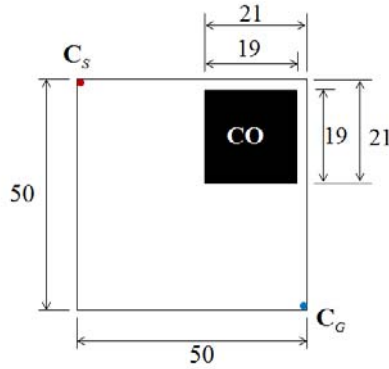


Figure 2.8 Fundamental example for a path planning

The work space of a path planning problem is defined as Fig. 2.8. As shown, the starting and goal point are located at the upper left corner and lower right corner respectively. The resulting path can be easily predicted; the path will be a straight diagonal line. The purpose of this simple problem is to examine the feasibility of the objective function. In addition, it can be proved whether the modified topology optimization algorithm described in previous sections is suitable for designing path or not.

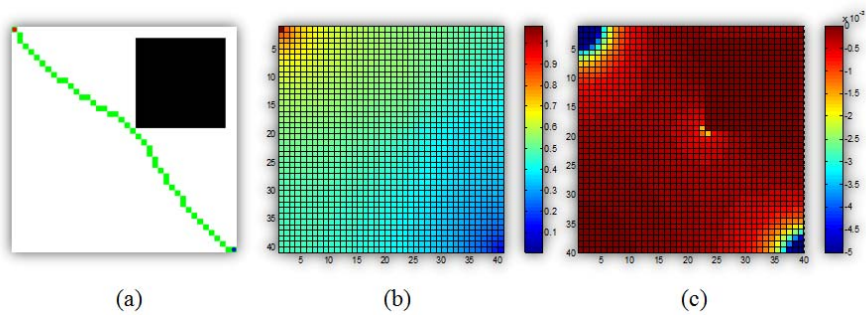


Figure 2.9 Results of problem of Fig. 2.8: (a) optimal path, (b) temperature distributions, and (c) sensitivities

The resulting path is shown in Fig. 2.9(a). The path of Fig. 2.9(a) does not look like a straight line. It should be understood as the numerical convergence error. The penalty exponent value of this example is given as a value of 3. The compliance minimization problem using the penalized interpolation method is basically non-convex problem with many local optimums.[58] The curved paths shown in Fig. 2.9(a) is local optimal solution originated from the non-convexity of the problem. To heighten the possibility of global optimal solution, we can use the continuation method. [58]. In continuation method, the value of the penalty exponent slowly increases. Figure 2.10 shows the improved results. Each penalty exponent vale is given at Table 2.3. As you see, the small value of penalty exponent at initial iterations clearly improves the resulting path. However, the computation cost has to be sacrificed.

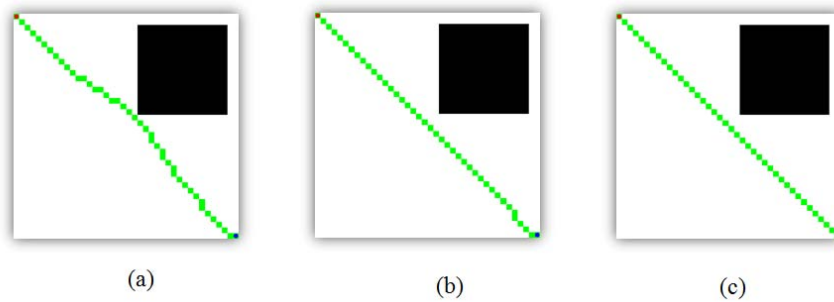


Figure 2.10 Improved paths by using continuation method. Each exponent penalties are given in Table 2.3

Table 2.3 Variations of penalty exponent in each case of Fig. 2.10

Fig. 2.10(a)	$P_i = \begin{cases} 1 & i \leq 20 \\ \min(3, 1 + 0.1 \times (i - 20)) & i > 20 \end{cases}$
Fig. 2.10(b)	$P_i = \begin{cases} 1 & i \leq 100 \\ \min(3, 1 + 0.1 \times (i - 20)) & i > 100 \end{cases}$
Fig. 2.10(c)	$P_i = \begin{cases} 1 & i \leq 100 \\ \min\left(3, 1 + 0.1 \times \text{floor}\left(\frac{i - 20}{3}\right)\right) & i > 100 \end{cases}$ where, $\text{floor}(x)$ means the nearest integers less than or equal to x .

2.3.2 Path planning avoiding obstacles

Obstacle free path planning algorithm will have to answer two kinds of questions: if there is a path, the algorithm has to find it. If it does not exist, the algorithm should report it. In the former case, there is no need to mention separately. However, in the later case, perception of the non-existence of the path is not easy. For this reason, very little work has addressed reporting the non-existence of the path. However, to ensure the perfection of the path planning algorithm, the reporting of non-existing path is a prerequisite that is very important and fundamental. Before a more detailed explanation about the reporting algorithm, let's compare two paths in Fig. 2.11.

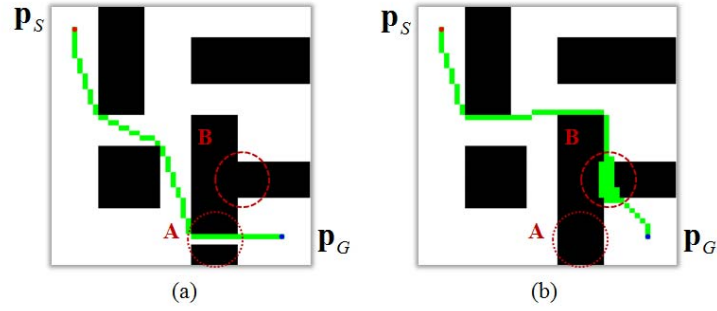


Figure 2.11 Paths generated in workspace (a) where a path exists and (b) where a path is not exist

The path in Fig. 2.13(a) is planned in the workspace with a narrow passage at region A. Regardless of the width of a passageway, if present, the proposed method should find that pathway. On the other hand, the workspace of Fig. 2.13(b) does not have a passage. However, as you can see, infeasible path penetrating an obstacle at region B is planned. This infeasible path is caused by the fact that obstacles are assigned by non-zero value of thermal conductivity. The reporting of non-existence uses this characteristic. When a path is given, non-existing of a path is verified by the following comparisons:

$$\begin{aligned}
 &\text{if } \Omega_p \cap \Omega_I = \emptyset, \text{ Then, Feasible path exists.} \\
 &\text{if } \Omega_p \cap \Omega_I \neq \emptyset, \text{ Then, Feasible path does not exist.}
 \end{aligned}
 \tag{2.33}$$

In the proposed path planning method, because the path is generated by consecutive finite elements, it is easy to extract the coordinates of the path elements and obstacle elements. And the comparison of Eq. (2.33) is executed by using the coordinate of each element.

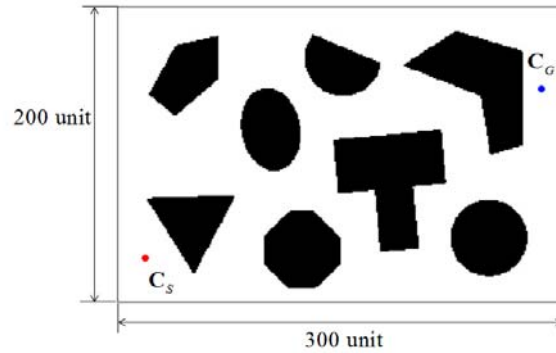


Figure 2.12 Work space with scattered polygonal obstacles

Figure 2.12 shows the work space in which scattered polygonal obstacles exist. The design space is divided into 60000 finite elements. The starting and goal point - dictated by C_s and C_g - are displayed by red and blue points. In addition, this section covers a point robot. Thus the size and orientation of the robot is not considered. So, the configuration space (C) is same as the work space (W). The resulting path is given in Fig. 2.13.

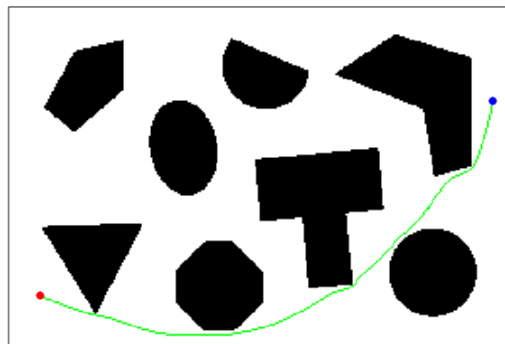


Figure 2.13 Optimal path of the problem of Fig. 2.12

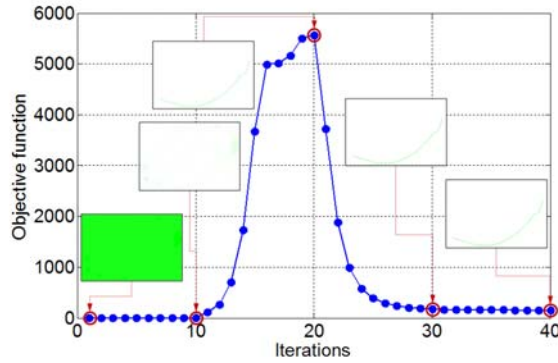


Figure. 2.14 Iteration histories of a result of Fig. 2.13

Figure 2.14 shows the iteration history. The objective function initially increased and then decreased again. This phenomenon is due to the mass constraint of Eq. 2.27. Because the allowable mass fraction was given a value of 1 at the beginning and then decreased, the objective function increased gradually until the allowable mass fraction reaches to M_{\min} . After that, the process where the distributed mass converges into 0 and 1 makes the objective function to be decreased. It is important thing that the presence of various obstacles does not affect the convergence speed and computation cost.

2.3.3 Continuous curvature path planning

In this section, the continuous curvature path is planned. In the case of a car-like robot, the movement and steering of a robot occurs simultaneously. So, the curvature of a path has to be changed continuously. Commonly, the continuous curvature path is obtained by smoothing a given path. Nevertheless, it is not easy to interpolate the graphical path composed by straight lines connecting two feasible waypoints. It is originated from the

sparsely and irregularly distributed waypoints. Generally, a continuous curvature smoothing method uses one of two kinds of curves: B-spline and Clothoid. Although B-spline curve is easy to implement, it is hard to limit the minimum curvature. On the other hand, Clothoid is hard to implement but has advantage in limiting the minimum curvature. [59] In recent years, Walton and Meek suggest a smoothing method using Clothoid curve systematically [60]. They classified clothoid blending into three kinds: Symmetric, Unsymmetric, and Circular blending. If the given three waypoints satisfy some specific conditions, the symmetric blending of clothoid is systematically determined. On the other hand, unsymmetric and circular blending is not easy and needs to iterative process to determine the curve. It means that the paths given by conventional path planning algorithm is not easy to apply clothoid blending systematically. However, because the path given by proposed method has consecutive waypoints, it is easy to apply the symmetric clothoid blending technique. To use the symmetric clothoid blending, three waypoints that are deployed in equal intervals should be given as shown in Fig. 2.15.

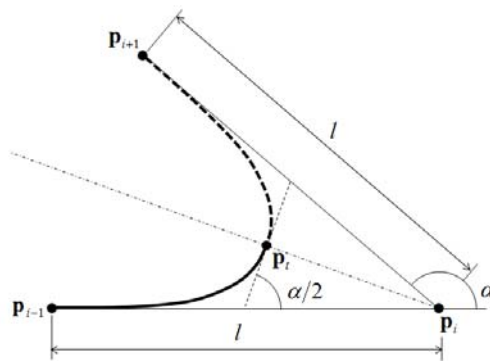


Figure 2.15 Interpretation of symmetric clothoid blending

If three waypoints deployed in equal intervals are given, to obtain the clothoid curve depicted by solid line connecting and \mathbf{p}_i is straight forward. So the more details are omitted. (See. [60]) In this thesis, we focus on how to determine the three waypoints deployed in equal interval.

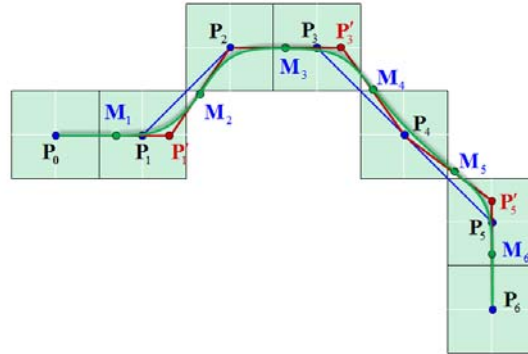


Figure 2.16 Determining of the triplete to be used for symmetric clothoid blending and the interpolated clothoid curve

Figure 2.16 shows how three waypoints are determined. \mathbf{p}_i , \mathbf{p}'_i , and \mathbf{M}_j are the center position vector of path elements and new position vector satisfying the equal distance condition, and midpoint of two selected center position vectors respectively. In conclusion, the path changes as follows:

$$\begin{aligned}
 \mathbf{P} &= [\mathbf{p}_0 \rightarrow \mathbf{p}_1 \rightarrow \mathbf{p}_2 \rightarrow \mathbf{p}_3 \rightarrow \mathbf{p}_4 \rightarrow \mathbf{p}_5 \rightarrow \mathbf{p}_6] \\
 &\quad \Downarrow \\
 \mathbf{P} &= [\mathbf{p}_0 \rightarrow \mathbf{p}'_1 \rightarrow \mathbf{p}_2 \rightarrow \mathbf{p}'_3 \rightarrow \mathbf{p}_4 \rightarrow \mathbf{p}'_5 \rightarrow \mathbf{p}_6] \\
 &\quad \Downarrow \\
 \mathbf{P} &= [\mathbf{p}_0 \rightarrow \mathbf{M}_1 \rightarrow \mathbf{M}_2 \rightarrow \mathbf{M}_3 \rightarrow \mathbf{M}_4 \rightarrow \mathbf{M}_5 \rightarrow \mathbf{M}_6 \rightarrow \mathbf{p}_6]
 \end{aligned}$$

As above mentioned, symmetric clothoid blending demands three waypoints deployed in equal intervals. So triplet of path elements is selected and interpolated. For example, in Fig. 2.16, three triplets can be obtained: $[p_0, p_1, p_2]$, $[p_2, p_3, p_4]$, and $[p_4, p_5, p_6]$.

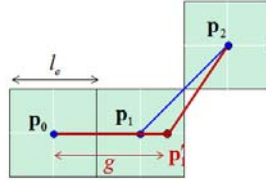


Figure 2.17 Triplet of path elements

Figure 2.17 shows how to smooth the path of the first triplet $[p_0, p_1, p_2]$. In Fig. 2.17, l_e and g are the edge length of finite element and given distance respectively. The predefined value g is very important value that determines the curvature of the path. Basically, the arrangement of the triplet of path elements is limited as four kinds shown in Fig 2.18.

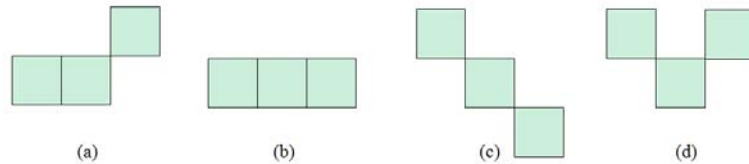


Figure 2.18 The kinds of arrangement of the triplet of path elements:

$$(a) g > (\sqrt{5}/2)l_e, (b) g > l_e, (c) g > \sqrt{2}l_e, \text{ and } (d) g > l_e$$

From the cases of Fig. 2.18, g is limited as follows:

$$\frac{\sqrt{5}}{2}l_e < g \quad (2.34)$$

However, the cases of Fig. 2.18(b) and 2.18(c) do not need smoothing. It can be simply defined as line segment. So, the interval g should be limited as:

$$g < 2l_e \quad (2.35)$$

Given waypoints $\mathbf{p}_0(x_0, y_0)$, $\mathbf{p}_1(x_1, y_1)$, $\mathbf{p}_2(x_2, y_2)$, and interval g , new waypoint \mathbf{p}'_1 rearranged on same interval g is

$$\mathbf{p}'_1 = (c_3 + c_5c_4, c_1c_3 + c_4c_5 + c_2) \quad (2.36)$$

where,

$$c_1 = -\frac{x_2 - x_0}{y_2 - y_0} \quad (2.37)$$

$$c_2 = \left(\frac{x_2 - x_0}{y_2 - y_0}\right)\left(\frac{x_2 + x_0}{2}\right) + \left(\frac{y_2 + y_0}{2}\right) \quad (2.38)$$

$$c_3 = -\frac{c_1(c_2 - y_0)^2 - x_0}{c_1^2 + 1} \quad (2.39)$$

$$c_4 = \frac{\sqrt{\{c_1(c_2 - y_0) - x_0\}^2 - (c_1^2 + 1)\{(c_2 - y_0)^2 + x_0^2 - g^2\}}}{c_1^2 + 1} \quad (2.40)$$

$$\left\{ \begin{array}{l} \text{if } \frac{(\mathbf{p}_2 - \mathbf{p}_1) \times (\mathbf{p}_1 - \mathbf{p}_0)}{\|(\mathbf{p}_2 - \mathbf{p}_1) \times (\mathbf{p}_1 - \mathbf{p}_0)\|} \bullet \frac{(\mathbf{p}_2 - \mathbf{p}_0) \times (\mathbf{p}'_1 - \mathbf{p}_0)}{\|(\mathbf{p}_2 - \mathbf{p}_0) \times (\mathbf{p}'_1 - \mathbf{p}_0)\|} = 1, \text{ Then, } c_5 = 1 \\ \text{if } \frac{(\mathbf{p}_2 - \mathbf{p}_1) \times (\mathbf{p}_1 - \mathbf{p}_0)}{\|(\mathbf{p}_2 - \mathbf{p}_1) \times (\mathbf{p}_1 - \mathbf{p}_0)\|} \bullet \frac{(\mathbf{p}_2 - \mathbf{p}_0) \times (\mathbf{p}'_1 - \mathbf{p}_0)}{\|(\mathbf{p}_2 - \mathbf{p}_0) \times (\mathbf{p}'_1 - \mathbf{p}_0)\|} = -1, \text{ Then, } c_5 = -1 \end{array} \right. \quad (2.41)$$

Equation (2.41) determines the sign of two real roots. If the new waypoint \mathbf{p}'_1 is obtained, then the midpoints \mathbf{M}_1 and \mathbf{M}_2 are obtained easily. And the angle α also can be calculated.

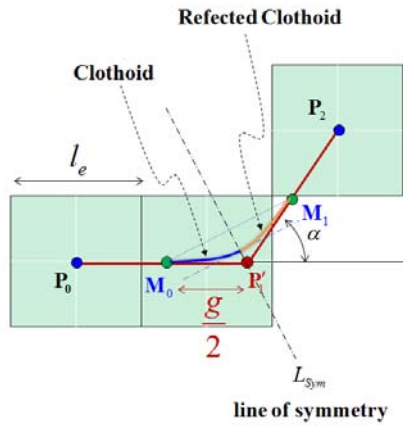


Figure 2.19 Analysis and interpolation of discretized path elements by using symmetric clothoid blending

Figure 2.19 shows the clothoid curve and its reflected curve. The symmetric clothoid blending means that the soothing is complete using two clothoid segments. The clothoid curve is determined as follows:

$$x(\theta) = \frac{a}{\sqrt{2\pi}} \int_0^\theta \frac{\cos u}{\sqrt{u}} du \quad (2.42)$$

$$y(\theta) = \frac{a}{\sqrt{2\pi}} \int_0^\theta \frac{\sin u}{\sqrt{u}} du \quad (2.43)$$

where variable θ exist in the interval $0 \leq \theta \leq \sqrt{\alpha/\pi}$. The angle α and scale factor a are determined as follows:

$$\alpha = \cos^{-1} \left(\frac{\|\mathbf{p}_2 - \mathbf{p}_0\|^2}{2g^2} - 1 \right) \quad (2.44)$$

$$a = \frac{1}{2} \frac{g}{C\left(\frac{\alpha}{2}\right) + S\left(\frac{\alpha}{2}\right) \tan\left(\frac{\alpha}{2}\right)} \quad (2.45)$$

In Eq (2.45), $C(\theta)$ and $S(\theta)$ is Fresnel's cosin and sine integral respectively. It can be computed numerically.

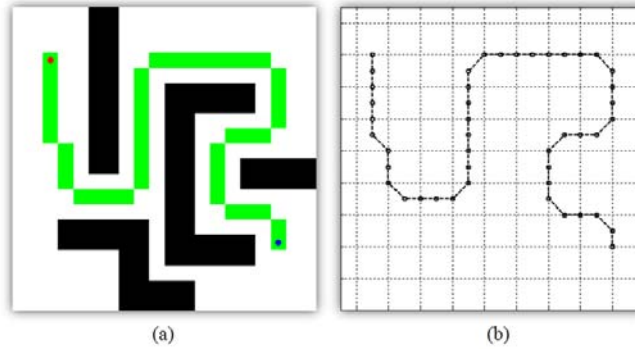


Figure 2.20 Numerical example: (a) path represented in design domain and (b) its graphical representation

Figure 2.20 shows numerical examples. Figure 2.20(a) is the optimal path planned by suggested method. Figure 2.20(b) is graphical representation of Fig. 2.20(a). The path is composed with many short line segments. Figure 2.21 is smoothing path using symmetric clothoid blending.

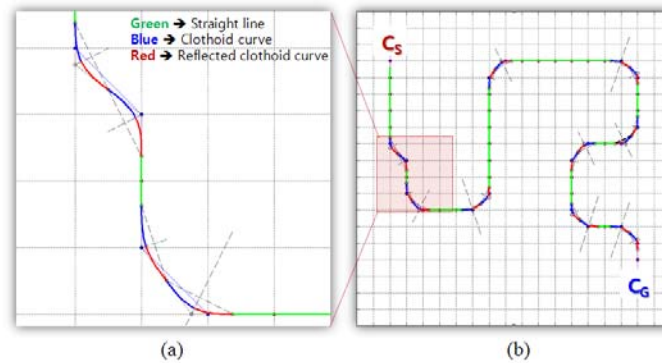


Figure 2.21 Clothoid curve interpolating the path of Fig. 2.22(b): (a) the enlarged part of Fig. 2.21(b) and (b) final smoothing path

Figure 2.21(b) is continuous curvature path smoothing the graphical path of Fig. 2.20(b). The enlarged part of red square region in Fig. 2.20(b) is shown in Fig. 2.21(a). The path is composed of three kinds of segments: straight line (Green), clothoid curve (Blue), and reflected clothoid curve (Red). Basically, the case of (b) and (c) of Fig. 2.18 are regarded as straight line segments.

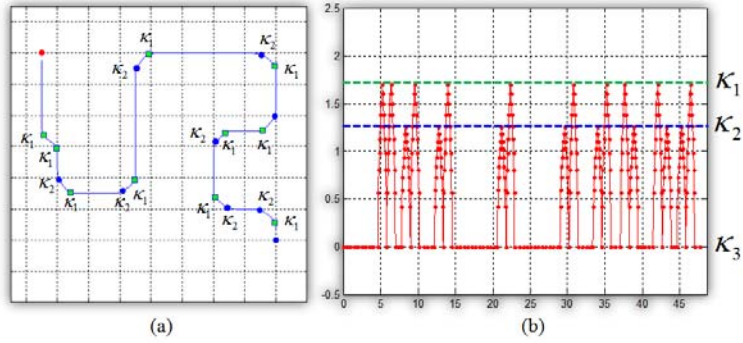


Figure 2.22 Curvature of the path of Fig. 2.23(b): (a) maximum curvature spot and (b) variations of curvature of whole path

The curvature of the path is shown in Fig. 2.22. The curvature κ is calculated as:

$$\kappa(\theta) = \frac{\sqrt{2\pi\theta}}{a} \quad (2.46)$$

The curvature is maximized where θ becomes maximum. The maximum curvature κ_{\max} is

$$\kappa_{\max} = \frac{2\sqrt{2}\sqrt[4]{\pi\alpha}}{g} \left(C\left(\frac{\alpha}{2}\right) + S\left(\frac{\alpha}{2}\right) \tan\left(\frac{\alpha}{2}\right) \right) \quad (2.47)$$

In given example, $\kappa_{\max} = 1.6941$. It is noticed that κ_{\max} is inversely proportional to the distance g . On the other hand, g is proportional to the element length l_e . So, we can conclude $\kappa_{\max} \propto 1/l_e$. It means that the maximum curvature is dependent on the element size. Finally, the effect of

distance g is considered. As mentioned earlier, the distance g should be predefined in the interval of Eq. (2.34) and (2.35).

Figure 2.23 shows the variations of the paths with varying distance g . The curvature of a smoothing path changes with varying distance g . However, unfortunately, the relation between the maximum curvature and distance is not clear. Because the controlling of the maximum curvature of the path is very important for a practical car-like, proposed smoothing technique should be improved in the future. Nevertheless, the clear and easy implementation of the technique is potentially very practicable.

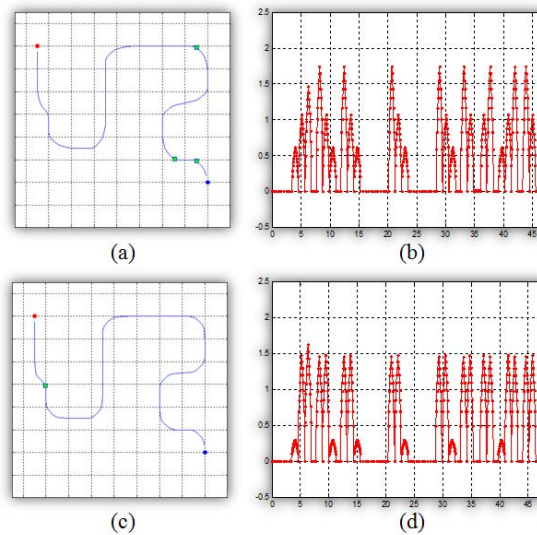


Figure 2.23 Paths with different control distance g : (a) interpolated path with $g = 1.15$ and (b) the curvature of it, and (c) interpolated path with $g = 1.20$ and (d) the curvatures of it

2.3.4 Obstacle free path planning of a square robot

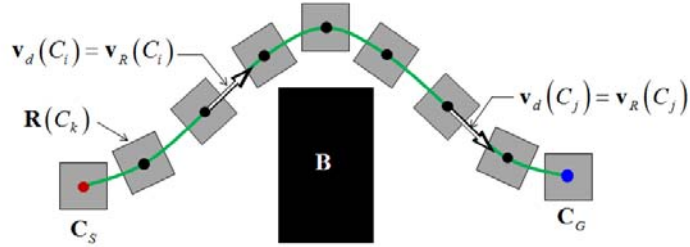


Figure 2.24 Moving square robot avoiding a rectangle obstacle

In this section, the size of the robot is considered as the key issue. To make it easier to explain, we will consider a rectangle robot first. Unlike the case of the point robot discussed in the previous section, the rectangle robot has the moving direction vector $\mathbf{v}_d(C_i)$, and orientation vector $\mathbf{v}_R(C_i)$ as shown in Fig. 2.24. In the case of rectangle robot, $\mathbf{v}_d(C_i)$ is same as $\mathbf{v}_R(C_i)$. Therefore, to obtain the configuration space \mathbf{C} , a rather complicated process is required. For example, the obstacles are magnified as much as the size of the robot shrinkage described in Section 2.2.1. In addition, the amount of the magnification varies depending on $\mathbf{v}_R(C_i)$. Typical solution is to build three-dimensional configurations space by considering the twist angle ϕ . Following Fig. 2.25 shows the three-dimensional configuration obstacles generated by twisting rectangle obstacle.

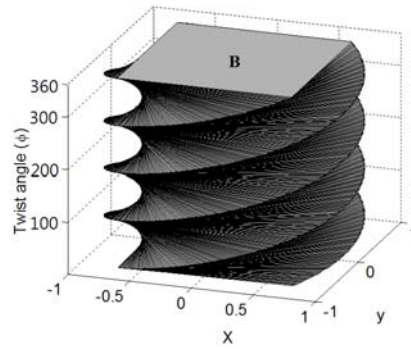


Figure. 2.25 Configuration space generated by twisting obstacle

However, if the shape of the obstacles or robot becomes more complex, constructing the configuration space using this technique becomes very difficult. In this thesis, simple feasibility check method will be used. The key advantage of our approach is that you do not have to twist the space. In addition, you can plan the path directly in the two-dimensional plane.

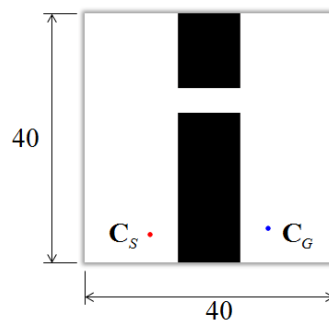


Figure. 2.26 Workspace for the rectangle robot's path planning

Figure 2.26 shows the work space of the rectangle robot. In this problem, the size of robot is defined as 2.5×2.5 units. 1 Unit means the size of a finite

Figure 2.28 shows the schematic of the planned path and a robot on the path. The green elements listed continuously indicate the generated path Ω_p . And the black elements partially listed at the top of the figure means the part of obstacle Ω_l . The feasibility of the path element Ω_i is determined as follow:

$$\begin{cases} \text{If } \mathbf{r}_j \in \Omega_l \text{ Then, } \Omega_i \equiv \Omega_l, \text{ where, } \Omega_l \text{ is an obstacle element.} \\ \text{If } \mathbf{r}_j \notin \Omega_l \text{ Then, } \Omega_i \equiv \Omega_p, \text{ where, } \Omega_p \text{ is an feasible path element.} \end{cases}$$

where \mathbf{r}_j are the point on the boundary of a robot layout. In other words, if \mathbf{r}_j is located at the obstacle element, then, the path element Ω_i , which including the smoothed curve $c(C_i)$, is defined as new obstacle element Ω_l . This process is completed by assign the thermal conductivity of Ω_i as $k_i \equiv \varepsilon \ll 1$. Following Fig. 2.29 shows the results of feasibility checking and new configuration space.

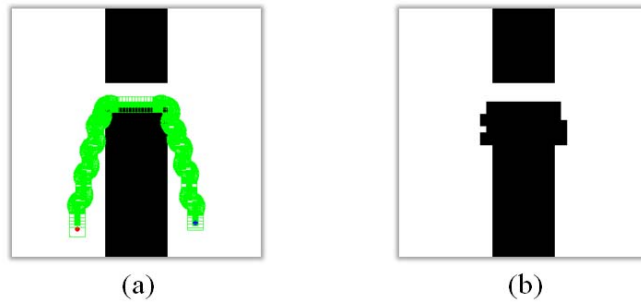


Figure 2.29 Feasibility checking: (a) physical poses of a robot on the path and (b) new configuration space

As you see in Fig. 2.29, compared with the original configuration space of Fig. 2.26, some new configuration obstacles are generated. The next step is nothing but a path generation in this new configuration space of Fig. 2.29(b). Figure 2.30 shows the results of the feasibility determination, reconstruction of a design domain, and path re-planning. Figure 2.30(a) is the planned path at a new configuration space. As shown in Fig. 2.30(b), No part of the path comes in contact with an obstacles.



Figure 2.30 Path planning on a new workspace of Fig. 2.29(b): (a) re-planned path and (b) physical poses of a robot on the path

Path planning in a more complex workspace shown in Fig. 2.31 is attempted. The design domain is divided into 150×100 units and the size of robot is 8×6 units. The path planning process is as same as described so far, so the result will be described briefly.

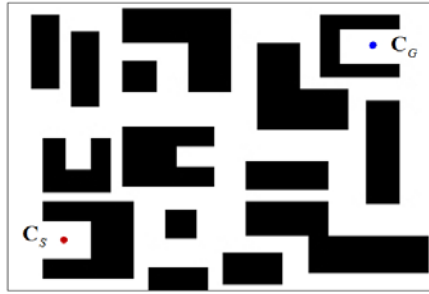


Figure 2.31 Workspace with complex obstacles

Figure 2.32 shows the first optimized path when the process of feasibility determination is not done yet. As expected, the presence of some areas where the path is in contact with the obstacles can be found. Thus, the path given above is inappropriate for use as the path of a robot.

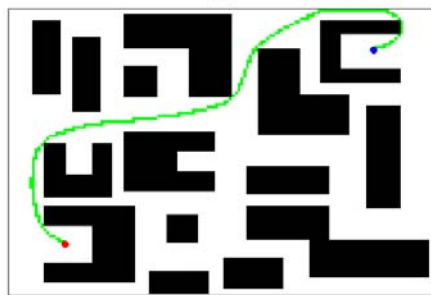


Figure 2.32 The first obstacle-free path

Figure 2.33 shows the re-constructed design domain after the 16 times of feasibility determination.

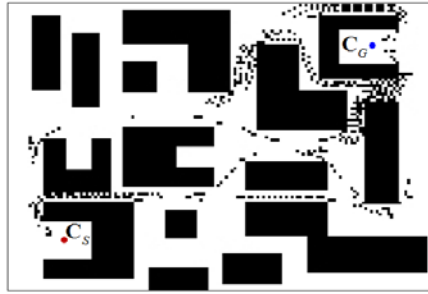


Figure 2.33 Design domain reconstructed after 16 times of feasibility determinations

Compared to the original design domain of Fig. 2.31, additional block elements can be found in the free design space.

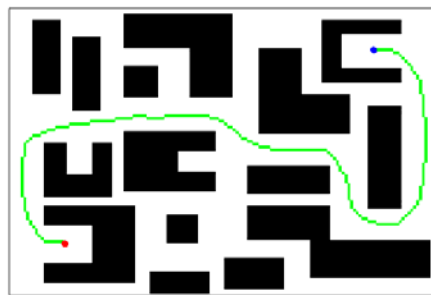


Figure 2.34 The final optimal path designed in workspace of Fig. 2.33

Figure 2.34 shows the optimized path designed in the design space of Fig. 2.33. Compared to the first optimal path shown in Fig. 2.32, the path is longer in length. However, it is clear that the above path has no contacts to the obstacles. The result of feasibility determination for the above path is given in Fig. 2.35. It can be found that the boundary of the robot also has no contacts to the obstacles.

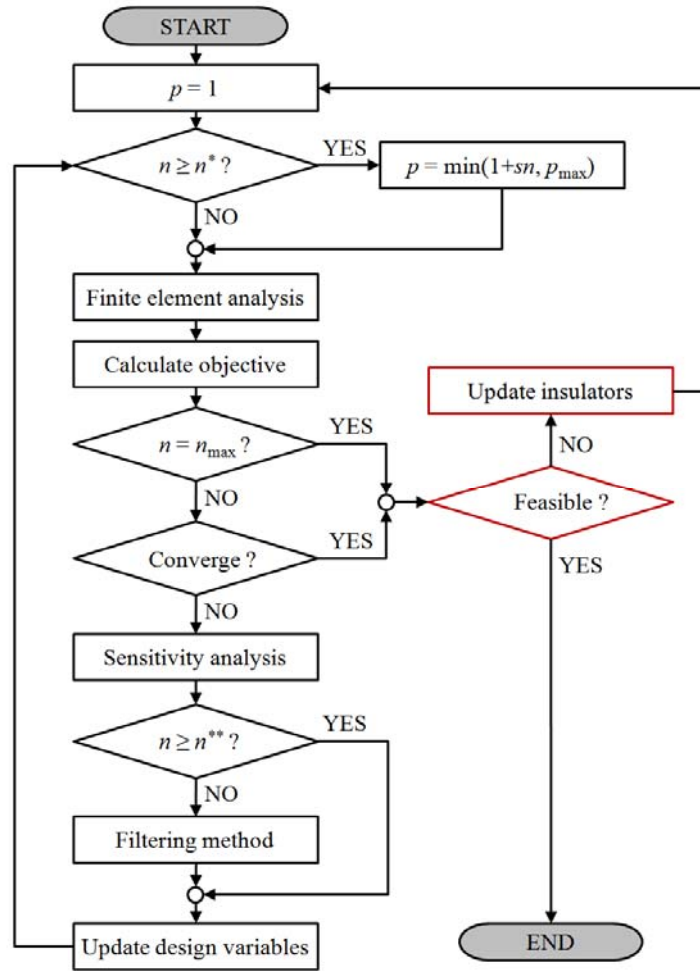


Figure 2.36 Flowchart of the process of feasibility determination

2.4 Outdoor global path planning

In this section, Outdoor global path planning will be presented. In the case of indoor global path planning described in Section 2.3, the most important thing is to design the path considering the size and orientation of the robot with obstacle avoidance. However, in the case of outdoor global path planning, because of the huge size of the workspace, a robot can be regarded as a point robot. In addition, the avoidance of obstacles such as lakes, rivers or buildings may be required by default. However, it may be more important to consider the condition of the terrain such as valley or slope of the surface.

This section will describe the method to design the path on the two-dimensional mapped space; the real terrain is mapped into the two-dimensional workspace. In particular, the height of the real terrain is represented by the thermal conductivity of the two-dimensional mapped work space.

2.4.1 Strategy for a mobility representation

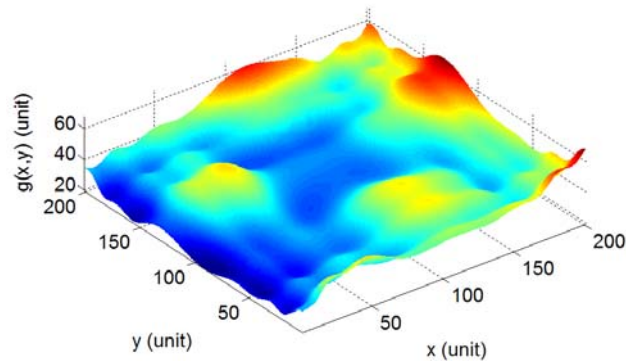


Figure 2.37 Surface $g(x, y)$ simulating a real terrain

Figure 2.37 shows the surface $g(x, y)$ simulating a real terrain. If the configuration C_i of a robot is determined by a position vector (\mathbf{P}_i) , C_i is indicated by following vector:

$$C_i = [x \quad y \quad g(x, y)]^T \quad (2.48)$$

As you can see in Eq. (2.48), the configuration of a robot belongs to the three-dimensional space; $C_i \in \mathbf{R}^3$. Thus, in order to use the algorithm mentioned until now, the configuration of Eq. (2.48) must be converted into the two-dimensional configuration. In other word, the mapping function F that maps $C_i \in \mathbf{R}^3$ into $C'_i \in \mathbf{R}^2$ should be defined. In conclusion, in this thesis, $F : C_i \rightarrow C'_i$ is defined as follows:

$$F(C_i) \equiv \begin{cases} x'_i = x_i \\ y'_i = y_i \\ k_x^i = f_x (dg(x_i, y_i)/dx_i) \\ k_y^i = f_y (dg(x_i, y_i)/dy_i) \end{cases} \quad (2.49)$$

Equation (2.49) indicates followings:

- x-y coordinates on surface of Fig. 2.37 is not changed.
- The height g of the surface of Fig. 2.37 is converted into the thermal conductivity through any transformation relation (f_x, f_y) .

As the transformation relation (f_x, f_y) , the following formula will be proposed:

$$k_x^i = k_x^0 / \sqrt{1 + (\partial g / \partial x)^2} ; k_y^i = k_y^0 / \sqrt{1 + (\partial g / \partial y)^2} \quad (2.50)$$

Equation (2.50) conceptually means that the thermal conductivity will be inversely proportional to the slope of the surface. For example, if $\partial g / \partial x$ and $\partial g / \partial y$ increase, the thermal conductivity becomes smaller. Eventually, that region becomes the insulation region. From the point of path planning, $\partial g / \partial x$ and $\partial g / \partial y$ indicates the level of ability to move of a robot at that region. For more details, consider Fig. 2.38.

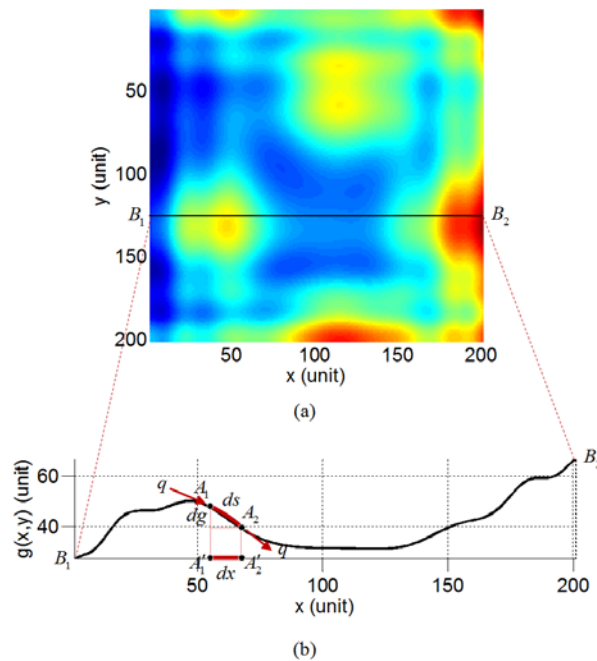


Figure 2.38 the relation between the thermal conductivity and the slope of the surface: (a) top view of the surface of Fig. 2.37 and (b) changes in topography of the cross section cut along $B_1 - B_2$

Figure 2.38(a) shows the top view of the surface $g(x, y)$. $g(x, 125)$ indicating the changes in topography of the cross section cut along $B_1 - B_2$ is shown in Fig. 2.38(b). Suppose two points presented as A_1 and A_2 on the curve $g(x, 125)$. The displacement ds between A_1 and A_2 is determined as following:

$$ds = dx\sqrt{1 + (dg/dx)^2} \quad (2.51)$$

Equation (2.51) indicates that all analysis will be carried out on the x coordinate line. Therefore, one can project A_1 and A_2 onto A'_1 and A'_2 on the x axis while imposing $T(A_1) = T(A'_1)$ and $T(A_2) = T(A'_2)$. If the amount of heat flux q is set to be equal in the original path $A_1 - A_2$ on the curve $g(x, 125)$ and projected path $A'_1 - A'_2$ on the x axis, one can use the following equation:

$$q = k_x^0 \frac{dT}{ds} = k_x \frac{dT}{dx} \quad (2.52)$$

Therefore, the projected problem onto the x axis becomes equivalent to the heat problem defined on a curve $g(x, 125)$. Combining the $dx - ds$ relation of Eq. (2.51) and Eq. (2.52) yields Eq. (2.50). Equation (2.50) indicates that as $\partial g/\partial x$ and $\partial g/\partial y$ becomes large, in example, as the height varies rapidly, small conductivity values are assigned to the corresponding elements.

2.4.2 Path planning in a simulated real terrain

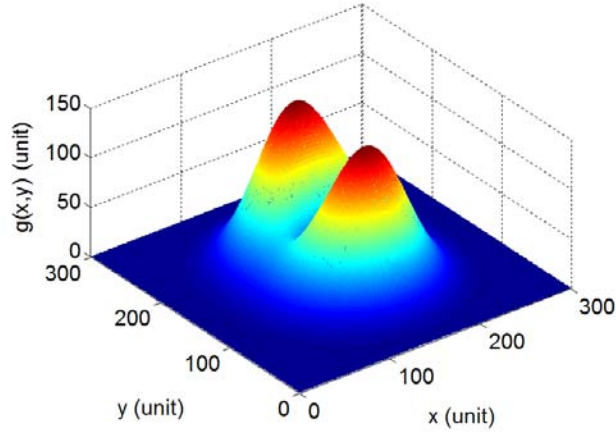


Figure 2.39 Simulated surface

As a specific case study, the simulated surface shown in Fig. 2.39 is considered. The simulated surface is defined by the following height function:

$$g(x, y) = \frac{1}{50}(x^2 + 3y^2)e^{1 - \left(\frac{x}{50}\right)^2 - \left(\frac{y}{50}\right)^2}; x, y \in [-150, 150]; x, y \in \mathbf{Z} \quad (2.53)$$

The thermal conductivity distributions of the simulated surface obtained by Eq. (2.50) are presented in Fig. 2.40. The nominal thermal conductivity is given as the value of 1 in here. As you can see in Fig. 2.40, the values of the thermal conductivity exist in the specific interval. Because the minimum value of the thermal conductivity is not a value of zero, a robot can move in the whole region.

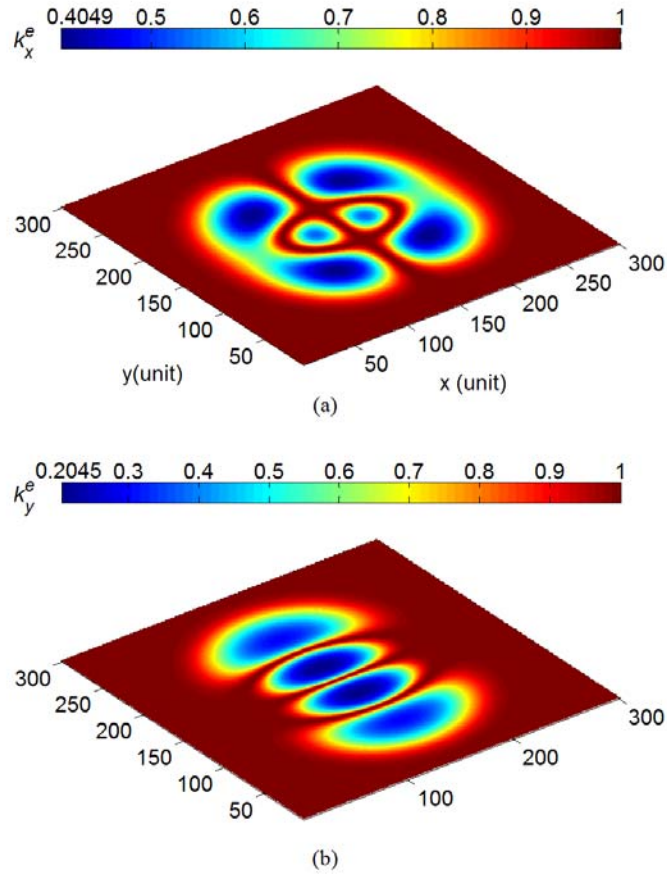


Figure2.40 The thermal conductivity given by Eq. (50). (a) k_x (x-directional thermal conductivity), (b) k_y (y-directional thermal conductivity)

Figure 2.41 shows the optimal path of a robot from C_S to C_G . The path is generated along the surface region where the variations of the slope are small.

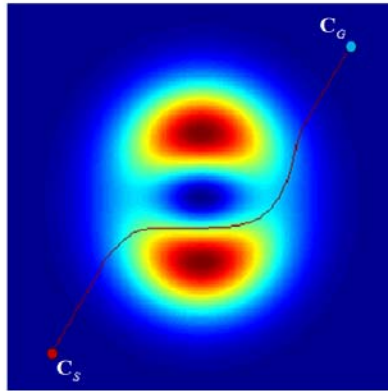


Figure 2.41 Optimal path in terrain of Fig. 2.39

To verify the validity of the algorithm, two simple paths shown in Fig. 2.42 will be compared. Figure 2.42(a) indicates the straight route connecting C_S and C_G . The path referred to as “Nominal 1”. Figure 2.42(b) indicates circular bypass route and referred to as “Nominal 2”.

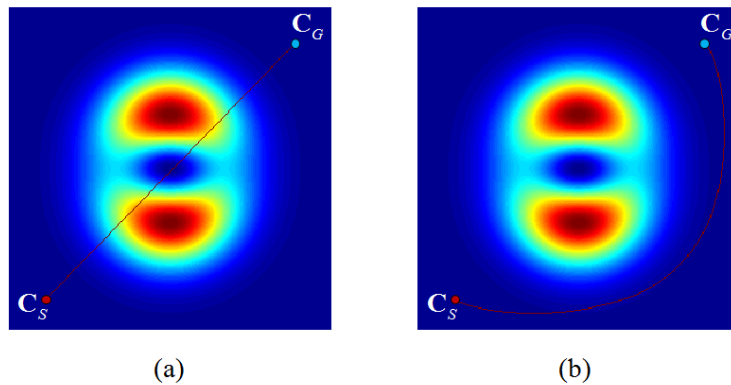


Figure 2.42 Intuitive simple paths for comparison with the path of Fig. 2.41; (a) straight route (Nominal 1), and (b) circular bypass route (Nominal 2)

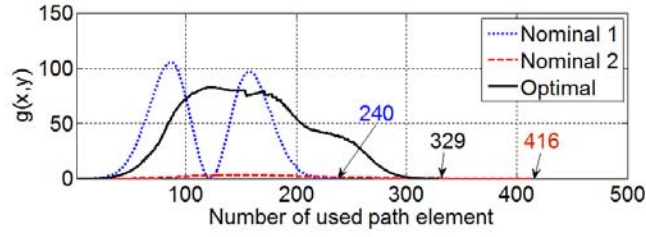


Figure 2.43 the variations of elevations $g(\mathbf{P}_i)$

Figure 2.43 shows the variations of $g(\mathbf{P}_i)$ along the each path. The x -axis indicates the number of path element. In the case of Nominal 1, the biggest change of elevation can be found. On the other hand, the smallest number of path elements is used. In the case of Nominal 2, the smallest change of elevations can be found. But, the largest number of path elements is used. The optimal path is positioned between them. For more accurate comparison, the cumulative distance D_{cumul} traveled over the simulated surface is calculated. The cumulative distance is calculated as:

$$D_{cumul} = \sum_{i=1}^{Ne-1} \sqrt{|\mathbf{P}_{i+1} - \mathbf{P}_i|^2 + |g(\mathbf{P}_{i+1}) - g(\mathbf{P}_i)|^2} \quad (2.54)$$

Where \mathbf{P}_i indicates the position vector of i -th element and $g(\mathbf{P}_i)$ means the elevation of the simulated surface at \mathbf{P}_i . Ne means the used number of element to form the path. Figure 2.44 shows the cumulative distance D_{cumul} .

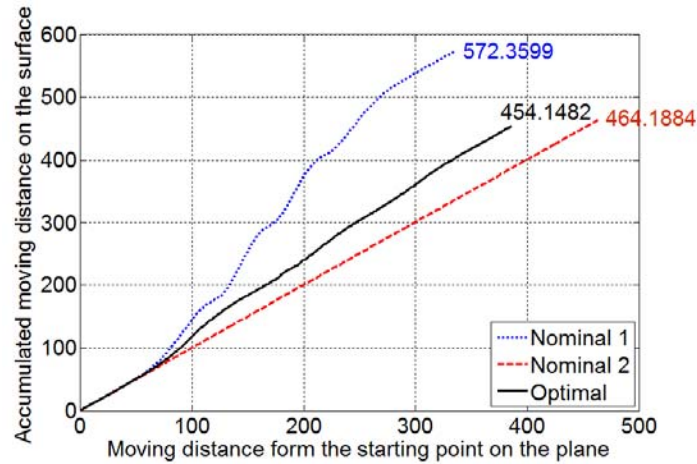


Figure 2.44 The cumulative distance traveled over the simulated surface

As you see in Fig. 2.44, the cumulative distance of the optimal path is smallest. Although Nominal 1 used the smallest number of path elements, the cumulative distance is largest. On the other hand, although Nominal 2 has a smallest change in pitch, the cumulative distance is larger than the optimal path.

2.4.3 Path planning in natural terrain represented by DEM

In previous section, to explain the characteristics of suggested method, mathematically continuous and differentiable surface function is used as the map. However the real natural terrain is just represented by the pixels with elevation. In this section, we will plan the shortest path on simple DEM.

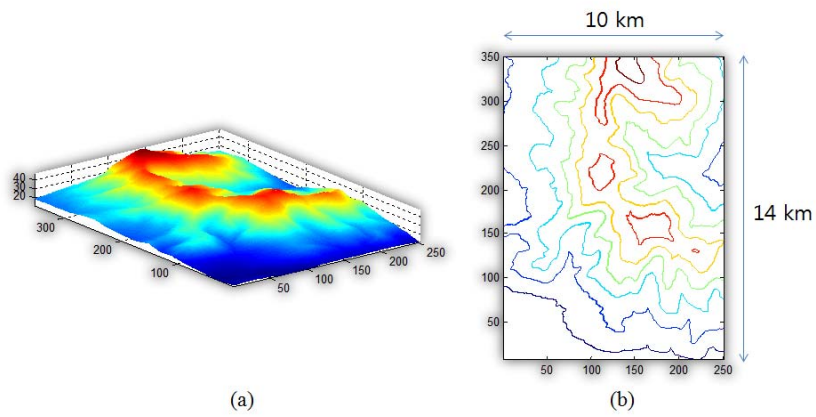


Figure 2.45 Natural terrain given in MATLAB: (a) 3D view and (b) contour map

Figure 2.45 is the real natural terrain map provided by MATLAB. The region is divided into 250×350 grid cells. The real size is about 10×14 km. So the grid size is about 40 m.

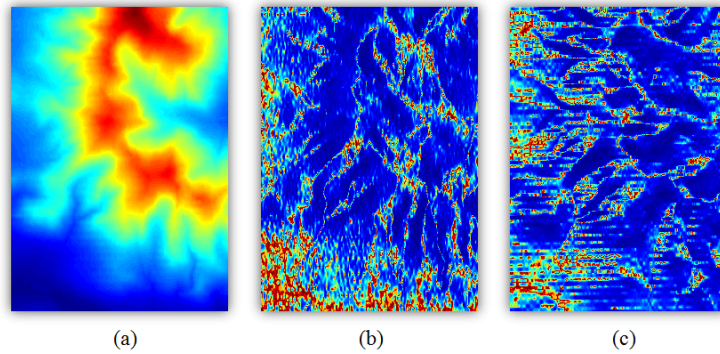


Figure 2.46 The distributions of the thermal conductivity: (a) top view of the terrain, and (b) x-directional and (c) y-directional conductivity

Figure 2.46 shows the thermal conductivity computed by the Eq. (2.50) with $k_0 = 1$. The differential values of elevations are obtained by numerically. The colors in Fig. 2.46(b) and Fig. 2.46(c) indicate the value of thermal conductivities. Closer to red is the color, closer to one the conductivity is.

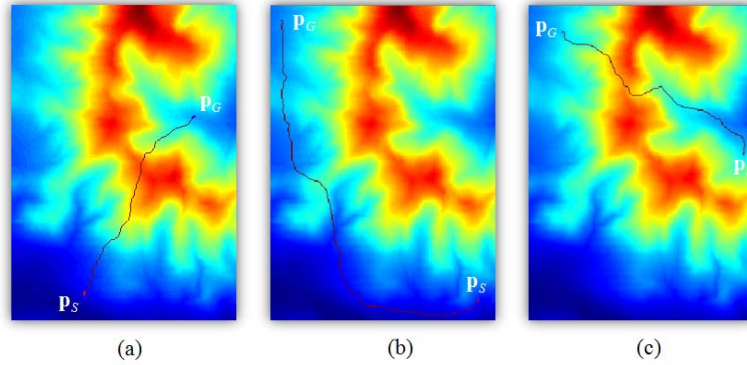


Figure 2.47 Paths planned in real terrain represented by DEM

Figure 2.47 shows different paths planned in natural terrain. Because no conditions are considered in the planning the paths, in some cases, paths overriding peaks are even formed. In practical, these kinds of paths are not desirable. Practical robots have the limitations of the slope angle to climb. So, technique to apply this limitation is needed. The algorithm of the maximum slope constraint would be very simple but effective. Because the thermal conductivity interpolation given in Eq. (2.50) is monotone decreasing function of the slope, the thermal conductivity can be easily re-determined. The minimum thermal conductivity $k(S_{\max})$ that converted from the maximum slope to climb is computed as:

$$k(S_{\max}) = k / \sqrt{1 + (S_{\max})^2} \quad (2.54)$$

where S_{\max} is simply the slope of the surface. Figure 2.54 is the DEM and elevation contour for an example.

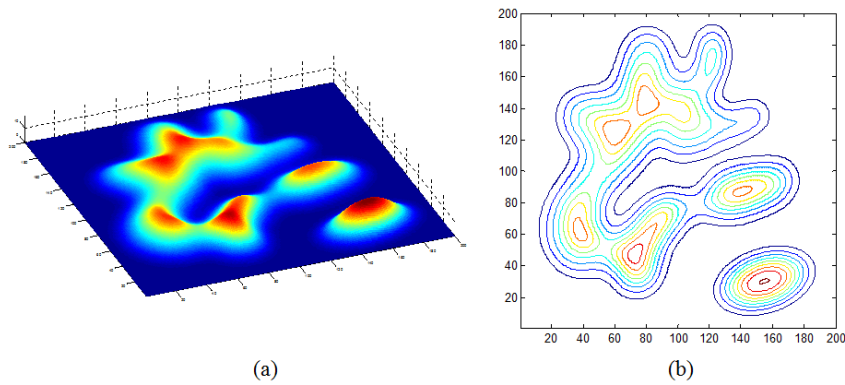


Figure 2.48 Example problem with the maximum slope constraints: (a) DEM and (b) its elevation contour map

The DEM of Fig. 2.48 is an artificially designed map. However, in contrast to example of Fig. 2.39, the map is constructed by using digital elevations not using the continuous function. The thermal conductivities when the allowed maximum slopes are 85° , 30° , and 15° respectively are showed in following Fig. 2.49. And the optimal paths at each case also displayed. As you see, lower the allowed slope, the pure obstacle regions are expanded. And the path passing through the plains is generated.

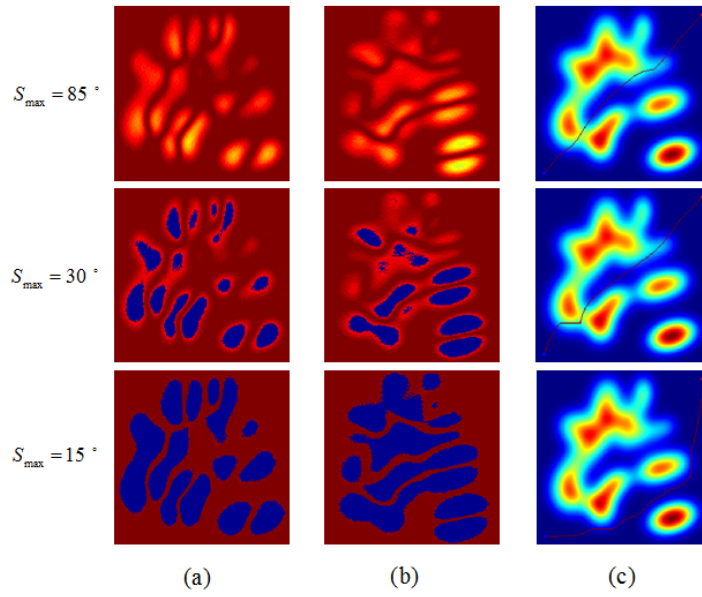


Figure 2.49 Thermal conductivity and planned paths: (a) x-directional and (b) y-directional thermal conductivities. (c) optimal paths

Figure 2.50 shows the comparison of the paths more clearly.

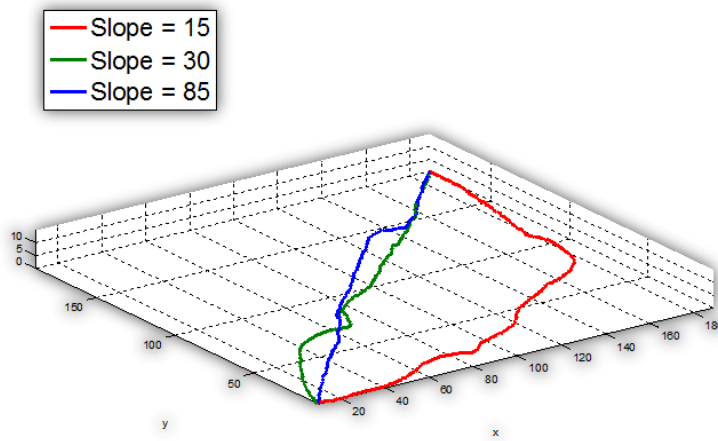


Figure 2.50 Comparison of three paths

Figure 2.51 shows the elevations and its derivatives. The derivatives of Fig. 2.51(b) are proposed as the thermal conductivity using Eq. (2.50). It should be noticed that one of two kinds of thermal conductivities - x/y-directional - should be in the interval expressed as yellow box of Fig. 2.51(b).

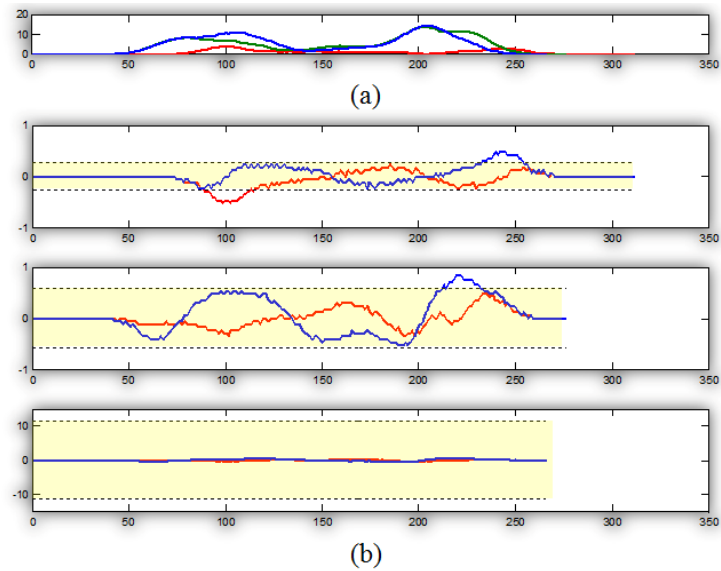


Figure 2.51 Variations of the (a) elevation and (b) thermal conductivity

2.5 Computation cost

The proposed method is very effective on the path planning itself. However, although the computation cost is not a critical issue in every path planning problems, it never be neglected. It is indisputable that the proposed method is disadvantages in computation time. The probabilistic road map method, which is based on the graphic search algorithm, is very fast. But it has probabilistic completeness and is a NP-hard. It means that the PRM is suitable to the local path planning. And in fact, it was used to plan the path in a small range. On the other hand, the proposed method based on topology optimization of compliance minimization is not NP-hard but a non-convex optimization problem. So, it may be more efficient than the PRM when the path should be planned in a large and complex workspace. In this section, we will just analyze the characteristics of computation cost of proposed method and seek the possibility of enhancement of it.

The proposed path planning algorithm has five kinds of important computation process as shown in Fig. 2.52: matrix assembly, solve the matrix equation, calculation of the objective function, analysis of sensitivities and filtering technique of the sensitivities.

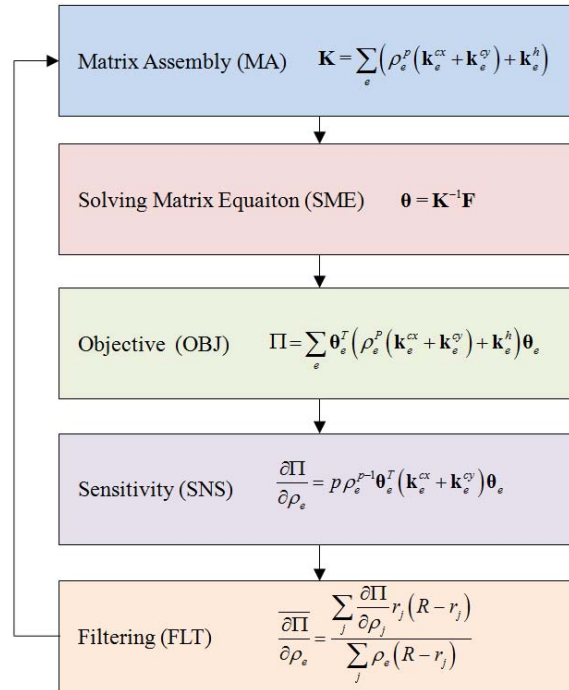


Figure 2.52 Computation process of a path planning based on topology optimization

The practical computation time is shown in Fig. 2.53. As mentioned above, proposed method is not NP-hard and the computation time is proportional to the size of design domain. Figure 2.55 is the results of the case where the size of a map is 100×100 . Numerical analysis was run on computer with Intel® Core™ i5-2500 3.3GHz quad-core process, 4GB RAM. The operation system is Window7 64bit.

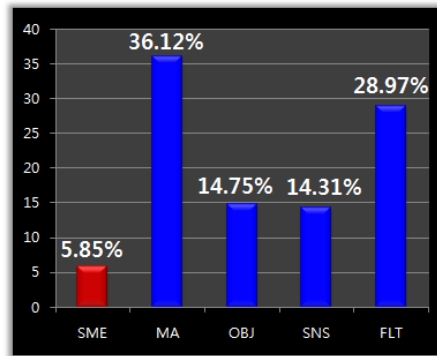


Figure 2.53 Computation cost of each computation process

As you can see, the assembly time is the most dominant. And the filtering time is second. The computation time of the objective function and sensitivities is same because the computation process is almost similar. Fortunately, the paralleled processing can be possible. For example, the time cost of assembly of element matrixes has been already reduced by parallel processing using multi-CPU. [41] Figure 2.54 shows the computation cost with the number of CPU.

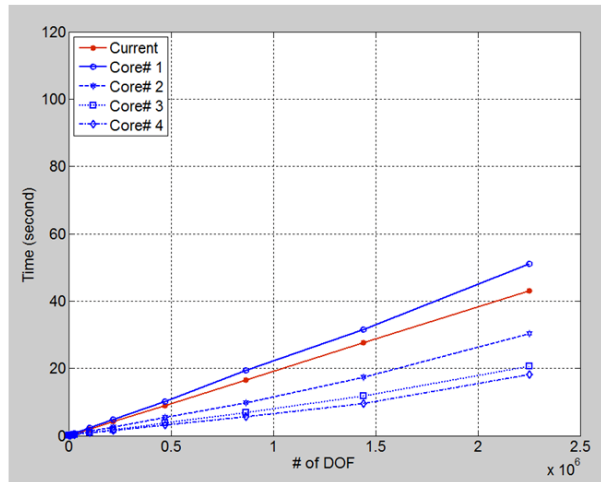


Figure 2.54 Comparison of computation cost with different number of CPU.

In Fig. 2.54, red solid line is the band matrix assembling used in proposed method. (It should be mentioned that the band matrix assembling is efficient for single core CPU. In the early study, the parallel processing had not been considered. So every numerical examples of this thesis are solved by the in house code using band matrix assembling technique for the assembly of global stiffness matrix) Figure 2.54 shows that the paralleled processing can reduce the assembling time. Paralleled processing can be also applied to other processes. Especially, the paralleled process using GPU can be used for the filtering process. By using CUDA, paralleled processing using GPU has been already used to reduce the computation time of various image filtering. Although the paralleled processing of the assembly of element matrix is tested only, it is clear that the computation cost of the proposed algorithm can be reduced. For more practical application, the algorithm should be improved by using paralleled processing.

2.6 Summary

A point robot path algorithm utilizing an analogy between the topology optimization of heat paths and robot path planning was newly developed. Although substantial advancements have been made in the field of topology optimization, there has been apparently no attempt to use newly developed topology optimization methods in robot path planning. In this respect, this work suggests new potential applications of topology optimization to non-traditional fields.

The analogy is based on the idea of viewing the start and goal points as a heat source and sink, respectively. No convection modeling is needed except for the goal points. When convection takes place as in the real physical world, numerical instability appears in the thermal topology optimization unless special treatment is given. In this respect, the employed conduction-dominant formulation can help yield stable numerical results. In employing the topology optimization method for path planning, the issue of assigning a mass constraint must also be addressed: in conventional topology optimization, one must provide a mass constraint. In robot path planning, however, it is not possible to select a specific upper bound on mass. We therefore propose a modified formulation that continuously reduces the mass upper bound as the iteration proceeds. Furthermore, the optimization is formulated so as to start with a full mass because it is difficult to select other bound values. This approach is shown to be effective through numerical examples. Due to the mass-constraint varying strategy, the convergence behavior of the objective function in the proposed planning problem is different from that typically

observed in conventional structural problems; in the present problems, the objective function value always increases at initial iteration steps and later reaches an optimal value. The developed algorithm yields stable, rapid solution convergence in all test problems. It is also effective in problems involving complex terrain conditions, where different complexity levels are modeled by different values of thermal conductivity. The problem on a real terrain was also effectively handled by relating terrain height derivatives to conductivity values.

Chapter 3

Variational Art

3.1 Hypothetical analogy

The main issue affecting use of the topology method for artistic or aesthetic applications is determining how to set up the topology optimization method because there is no real physical problem involved in image generation. For this reason, a hypothetical analogy is proposed to link topology optimization and image creation.

The underlying hypothesis is as follows. A brush stroke made on a canvas by an artist is viewed as a heat path optimally connecting a heat source and a heat sink in a two-dimensional plate under a mass constraint. Figure 3.1 is a schematic explanation of this analogy. The starting point of the brush stroke is viewed as a heat source while the ending point, as a heat sink. A thermal system compared to a set of strokes on a canvas will be called a virtual physical system in order to emphasize the fact that boundary and loading conditions for the system need not be realistic (e.g., hundreds of sources and sinks of arbitrary strength can be randomly distributed in the plate). By varying the mass constraint ratio assigned for the optimal heat-path finding problem, different optimal heat path shapes can be obtained. Obviously a straight line would be the most efficient heat path connecting a source and a sink if the mass constraint ratio is very tight. (The optimal path in the virtual

system will be found as a solution to the thermal compliance-minimizing topology optimization problem, but the detailed algorithm will be given in the next section.)

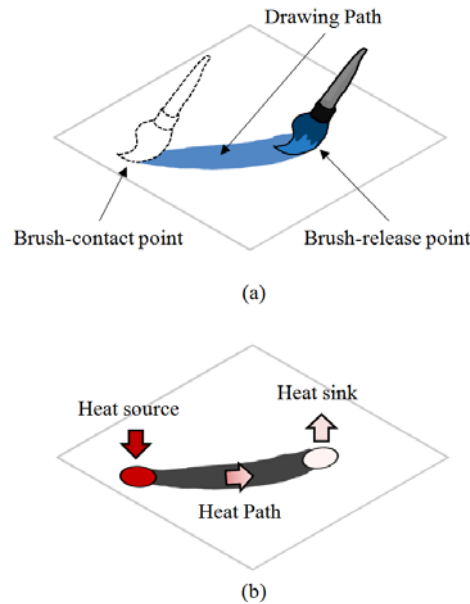


Figure 3.1 Hypothetical analogy between (a) brush strokes in painting and (b) the topology optimization problem to find an efficient heat dissipating path on a two-dimensional heat-conducting plate.

While the analogy plays a crucial role in creating aesthetic images, there is a fundamental difference between strokes made by a human and optimized heat path in that a human normally repeats a number of single strokes in a painting, but multiple heat sinks and sources can be assigned in the virtual heat-transfer system, yielding multiple optimized paths. In fact, the difference allows great freedom in generating a variety of images. Figure 3.2 is a conceptual illustration of multiple heat sinks and sources. Furthermore,

diverse images can be created if the locations of the sinks and sources are randomly selected.

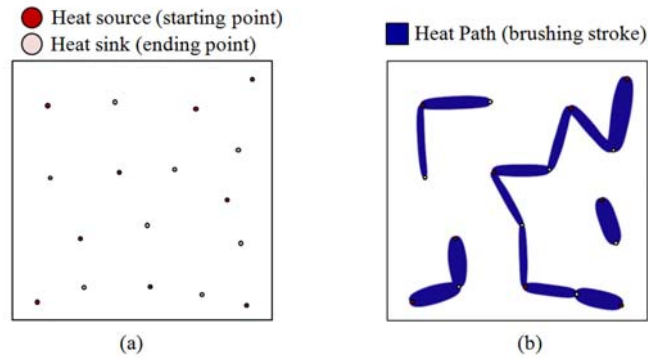


Figure 3.2 Simultaneous generation of multiple heat paths when multiple heat sources and sinks are used. (a) An example of distributed heat sinks and sources and (b) multiple optimized paths.

Key aspects of the proposed variational art algorithm are summarized below.

- 1) A brushing stroke on a canvas is viewed as an optimized path connecting a heat sink and a heat source for a given two-dimensional design domain of a heat-conducting plate under a mass constraint.
- 2) The optimization problem is formulated as a topology optimization problem to minimize thermal compliance.
- 3) Although the thermal compliance minimization that is compared to the act of brushing involves the physics of conduction and convection, arbitrariness in the number and locations of heat sinks/sources allows much freedom in generating various images.
- 4) Because the heat transfer problem is only a hypothetical analogy problem,

there is no need to obtain clearly-identifiable paths as required in topology optimization for real physical systems. Thereby, a touch ink-and-wash painting could be also realized.

3.2 Variational Art Algorithm

The variational art algorithm is basically the same as the topology optimization algorithm used to find efficient heat dissipating paths on a two-dimensional structure for a given set of heat sinks and sources and allowable mass usage. To model heat transfer phenomena, only steady-state conduction and normal convection will be considered. The virtual system used for image creation is schematically shown in Fig. 3.3.

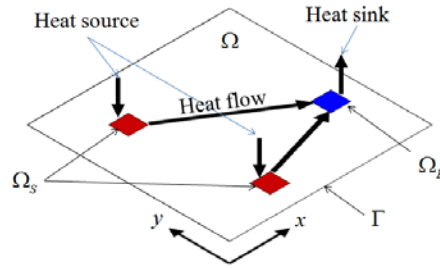


Figure 3.3 Virtual system of heat transfer that is used to develop the variational art algorithm.

Since heat transfer problems are solved by the variational art algorithm based on the topology optimization algorithm, we will simply use the same field variables as those used for topology optimization of optimal heat dissipating structures. Following the formulation given in an earlier work [24], we begin with the governing differential equation for a steady-state temperature field $\theta(x, y)$ on a two-dimensional plate Ω :

$$k(x, y)\nabla^2\theta(x, y) - h(x, y)\theta(x, y) + Q(x, y) = 0 \text{ on } \Omega \quad (3.1)$$

In Eq. (3.1), The variable $\theta(x, y) = T(x, y) - T_\infty$ actually implies an excess temperature part of $T(x, y)$ where T_∞ is viewed as an ambient temperature. The symbols $k(x, y)$ and $h(x, y)$ are the coefficients of thermal conductivity and convective heat transfer. Heat sources are denoted by $Q(x, y)$ prescribed on $d\Omega^S$ as

$$Q = Q^* \text{ in } \Omega_S \quad (Q = 0 \text{ elsewhere in } \Omega) \quad (3.2)$$

On the other hand, the value of the coefficient of convective heat transfer is used to model heat sinks such that

$$h = h^* \text{ in } \Omega_E \quad (h = 0 \text{ elsewhere in } \Omega) \quad (3.3)$$

As for the boundary condition on boundary Γ , the following Neumann-type condition is used although other conditions may be employed:

$$-k\nabla\theta \cdot \mathbf{n} = 0 \text{ at } \Gamma \quad (3.4)$$

The problem defined by Eq. (3.1) through Eq. (3.4) is solved by the finite element method. Therefore, the region Ω where heat transfer takes place (shown in Fig. 3.3) is discretized by two-dimensional finite elements as illustrated in Fig. 3.4.

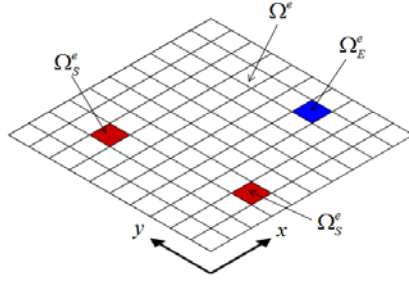


Figure 3.4 Discretized model of the virtual physical system

By following the standard finite element procedure [61], a system of matrix equations can be obtained

$$\mathbf{K}\boldsymbol{\theta} = \mathbf{F} \quad (3.5)$$

where symbols \mathbf{K} , $\boldsymbol{\theta}$ and \mathbf{F} denote the stiffness matrix, the nodal temperature vector and the load vector. If Ω is discretized by N_e finite elements, \mathbf{K} , $\boldsymbol{\theta}$ and \mathbf{F} are assembled using element-level matrices (${}^d\mathbf{K}^e$, ${}^v\mathbf{K}^e$) and vectors ($\boldsymbol{\theta}^e$, \mathbf{F}^e) where e denotes the element number.

$$\mathbf{K} = \sum_{e=1}^{N_e} {}^d\mathbf{K}^e + \sum_{e=1}^{N_e} {}^v\mathbf{K}^e \quad (3.6)$$

$$\mathbf{F} = \sum_{e=1}^{N_e} \mathbf{F}^e \quad (3.7)$$

$$\boldsymbol{\theta} = \sum_{e=1}^{N_e} \boldsymbol{\theta}^e \quad (3.8)$$

If linear interpolation functions used for four-node finite element discretization are denoted by N_i ($i=1,2,3,4$), the components of the element conduction matrix (${}^d\mathbf{K}^e$) and the element convection matrix (${}^v\mathbf{K}^e$) are given

as:

$${}^d K_{ij}^e = \int_{\Omega^e} \left(k^e \frac{\partial N_i}{\partial x} \frac{\partial N_j}{\partial x} + k^e \frac{\partial N_i}{\partial y} \frac{\partial N_j}{\partial y} \right) d\Omega^e \quad (3.9)$$

$${}^v K_{ij}^e = h^e \int_{\Omega^e} N_i N_j d\Omega^e \quad (3.10)$$

The values of element-level conduction coefficients are determined by Eq. (3.3). The components of the element force vector \mathbf{F}^e are expressed as

$$f_i^e = \int_{\Omega^e} N_i Q d\Omega^e \quad (i=1,2,3,4) \quad (3.11)$$

where the value of Q is determined by Eq. (3.2). Once the discretized system is modeled by the finite element equation (Eq. (3.5)), the following minimization problem is set up to find optimal paths of efficient heat dissipation:

$$\underset{(\rho_1, \rho_2, \rho_3, \dots, \rho_e)}{\text{minimize}} \quad \Pi = \boldsymbol{\theta}^T \mathbf{K} \boldsymbol{\theta} \quad (3.12)$$

$$\sum_{e=1}^{Ne} \rho_e m_e - M \leq 0 \quad (3.13)$$

$$0 < \varepsilon \leq \rho_e \leq 1 \quad (e=1,2,\dots,Ne; \varepsilon = \text{small nonzero value}) \quad (3.14)$$

The mass constraint is given by Eq. (3.13) where M is the mass allowed in forming heat paths and m_e is the element mass. The symbol ρ_e is a dimensionless design variable representing the relative density. For the

topology optimization setup, the element conductivity coefficient k^e appearing in Eq. (3.9) is interpolated in terms of the design variable ρ_e . In this study, the following polynomial interpolation [55] is employed:

$$k^e = k_e \rho_e^p \quad (3.15)$$

where k^e is the thermal conductivity of the e -th element and p is the penalty exponent. To solve the topology optimization using a gradient-based optimizer such as the OC (optimality criterion) algorithm, the following expression for the sensitivity of the objective function Π is needed:

$$\frac{\partial \Pi}{\partial \rho_e} = (\boldsymbol{\theta}^e)^T \frac{\partial \mathbf{K}^e}{\partial \rho_e} (\boldsymbol{\theta}^e) \quad (3.16)$$

Filtering may be used if necessary. For instance, one can use the following filter [61]:

$$\frac{\partial \Pi}{\partial \rho_e} = \frac{\sum_{j=1}^{N_s} \frac{\partial \Pi}{\partial \rho_j} \rho_j (R - r_j)}{\sum_{j=1}^{N_s} \rho_j (R - r_j)} \quad (3.17)$$

where R is the selected value of the filter radius, r_j is the distance between Ω^e and the j -th adjacent element and N_s is the total number of adjacent elements used for filtering.

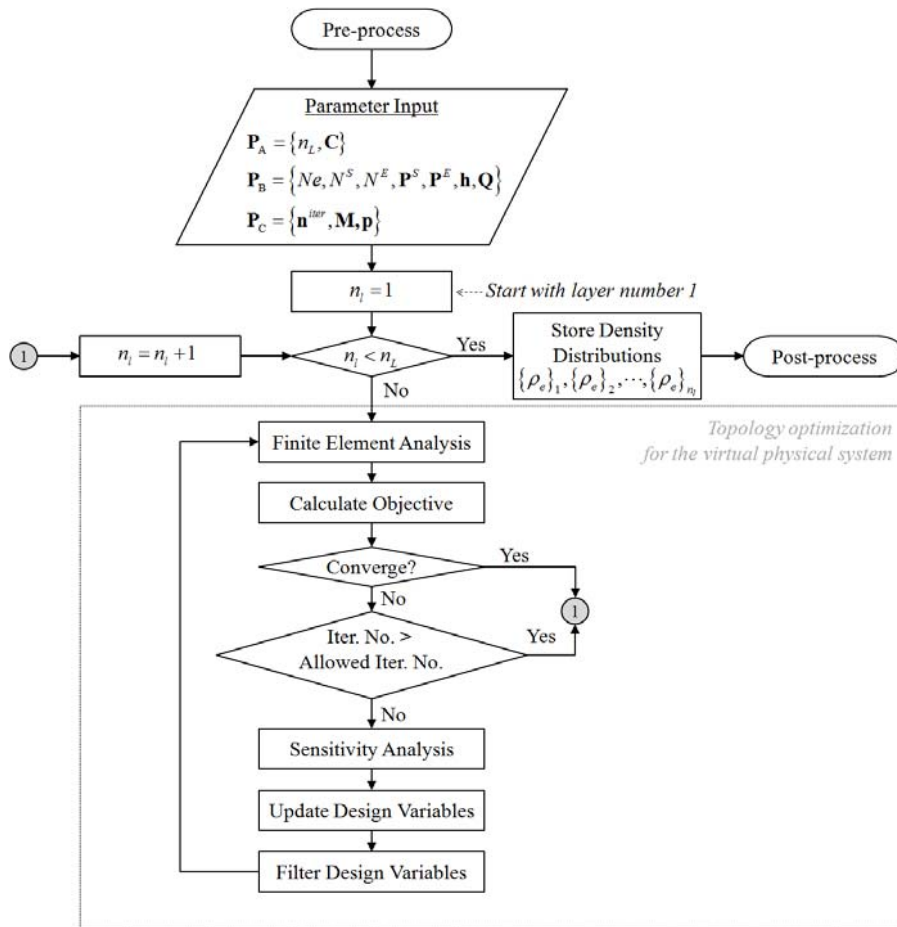


Figure 3.5 Flow chart of the proposed variational art algorithm

To give an overview of how the variational algorithm is implemented, the algorithm flowchart is given in Fig. 3.5. To run the variational art algorithm, three groups of parameters, \mathbf{P}_A , \mathbf{P}_B and \mathbf{P}_C (as indicated in Fig. 3.5), should be provided as input. The characteristics of the three groups are explained in Table 3. Table 3 lists all parameters needed to use the variational art algorithm.

Table 3.1: Parameters used in the variational art algorithm

Parameter group	Parameters
\mathbf{P}_A	n_L : Number of color layers to be used $\mathbf{C} = \{\mathbf{C}^1, \mathbf{C}^2, \dots, \mathbf{C}^L\}$: RGB triplets
\mathbf{P}_B	N_e : Number of elements (pixels) N^S : Number of heat sources (starting point) N^E : Number of heat sinks (ending point) $\mathbf{P}^S = \{\mathbf{P}_1^S, \mathbf{P}_2^S, \dots, \mathbf{P}_{N^S}^S\}$: Heat source locations (starting points) $\mathbf{P}^E = \{\mathbf{P}_1^E, \mathbf{P}_2^E, \dots, \mathbf{P}_{N^E}^E\}$: Heat sink locations (ending points) $\mathbf{h}^* = \{h_1^*, h_2^*, \dots, h_{N^E}^*\}$: Convection coefficients corresponding to heat sinks \mathbf{P}^E $\mathbf{Q}^* = \{Q_1^*, Q_2^*, \dots, Q_{N^S}^*\}$: Heat generation values corresponding to heat sources \mathbf{P}^S
\mathbf{P}_C	$\mathbf{n}^{iter} = \{n_1^{iter}, n_2^{iter}, \dots, n_{N_L}^{iter}\}$: The maximum allowed iteration number for layers $\mathbf{M} = \{M_1, M_2, \dots, M_{N_L}\}$: The allowed mass fractions for layers $\mathbf{p} = \{p_1, p_2, \dots, p_{N_L}\}$: The penalty parameters for layers

Figure 3.6 illustrates how a multi-color image (for $n_L > 1$) is created. As illustrated in Fig. 3.6, topology optimization problems are solved by n_L times. The converged images obtained for n_L layers are then superposed to make the final image. The detailed procedure for generating images from the results of topology optimization will be given in the next section as well as the image superposition technique.

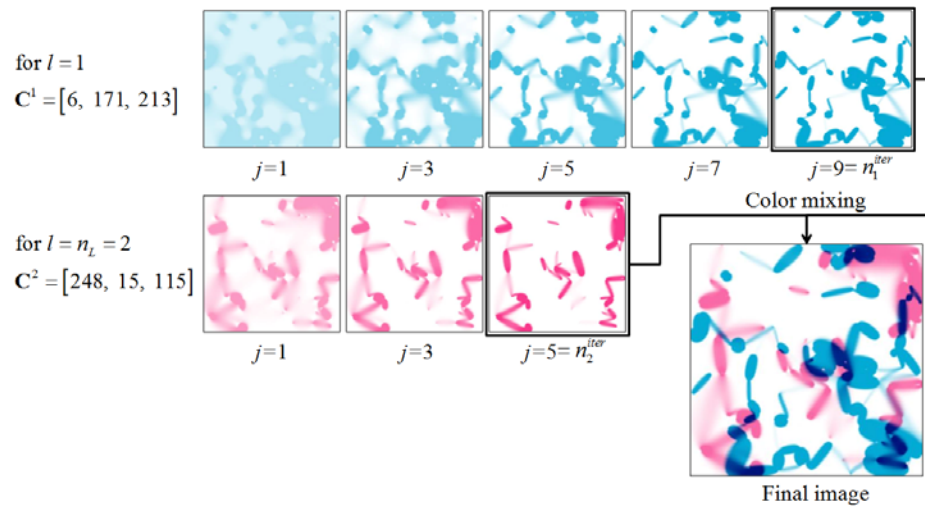


Figure 3.6 Schematic description of the creation of a multi-color image for $n_L = 2$. The final image is obtained by a color mixing technique (j : iteration number).

3.3 Parameters affecting image output

Images obtained by the proposed variational algorithm will be affected by the parameters introduced in Table 1. The image coloring technique is presented in this section, and the effects of other parameters on image output are discussed.

3.3.1 Coloring technique

The number of colors used is determined by $n_L \in \mathbf{P}_A$. The color of each finite element (or pixel) is represented by the RGB color model expressed by the triplet \mathbf{C}^l such that

$$\mathbf{C}^l = [r^l, g^l, b^l] \quad (l=1,2,\dots,n_L), \quad (3.18)$$

where r^l , g^l and b^l take on integer values between 0 and 255. If the e -th finite element occupying Ω_e has a density of ρ_e^l for the l -th color layer, then the color triplet \mathbf{C}_e^l will be defined as

$$\mathbf{C}_e^l = 255\mathbf{1} - \rho_e^l (255\mathbf{1} - \mathbf{C}^l) \quad (e=1,2,\dots,Ne; l=1,2,\dots,n_L), \quad (3.19)$$

where $\mathbf{1} = [1,1,1]$. The reason for defining the element color triplet using Eq. (3.19) instead of the simpler expression, $\mathbf{C}_e^l = \rho_e^l \mathbf{C}^l$, is that Eq. (3.19) assigns $[255,255,255]$ for $\rho_e^l \rightarrow 0$. This means that the corresponding element has

no color when $\rho_e^l \rightarrow 0$. Figure 51 illustrates how element colors are varied by the strategy in Eq. (3.19) as a function of the element density ρ_e .

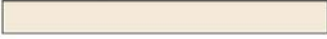
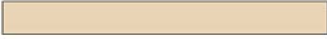
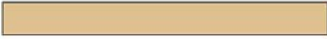
ρ_e^l	\mathbf{C}_e^l	
0.0	[0, 0, 0]	
0.2	[40, 30, 14]	
0.4	[80, 60, 28]	
0.6	[120, 90, 42]	
0.8	[160, 120, 56]	
1.0	[200, 150, 70]	

Figure 3.7 The color variation in an element according to Eq. (3.19) (the color triplet \mathbf{C}_e^l is arbitrarily chosen as [200,150,70]).

As shown Fig. 3.7, the value of ρ_e^l controls the shade of the element color. Once \mathbf{C}_e^l is determined for all elements ($e=1, \dots, Ne$) for all color layers ($l=1, \dots, n_L$), the n_L results can be superposed. Here, we propose the following color superposition method:

$$\mathbf{C}_e \equiv 255\mathbf{1} - \min\left(255\mathbf{1}, \sum_{l=1}^{n_L} (255\mathbf{1} - \mathbf{C}_e^l)\right), \quad e = 1, \dots, Ne \quad (3.20)$$

The superposition in Eq. (3.20) is based on the subtractive color mixture but it ensures that any value in the color triplet is not negative and also that [255,255,255] is assigned if $\sum \rho_e^l \rightarrow 0$. Figure 3.8 illustrates the superposed images generated by Eq. (3.20) for $n_L = 3$. The images in the last row represent the superposed images for each optimization iteration.

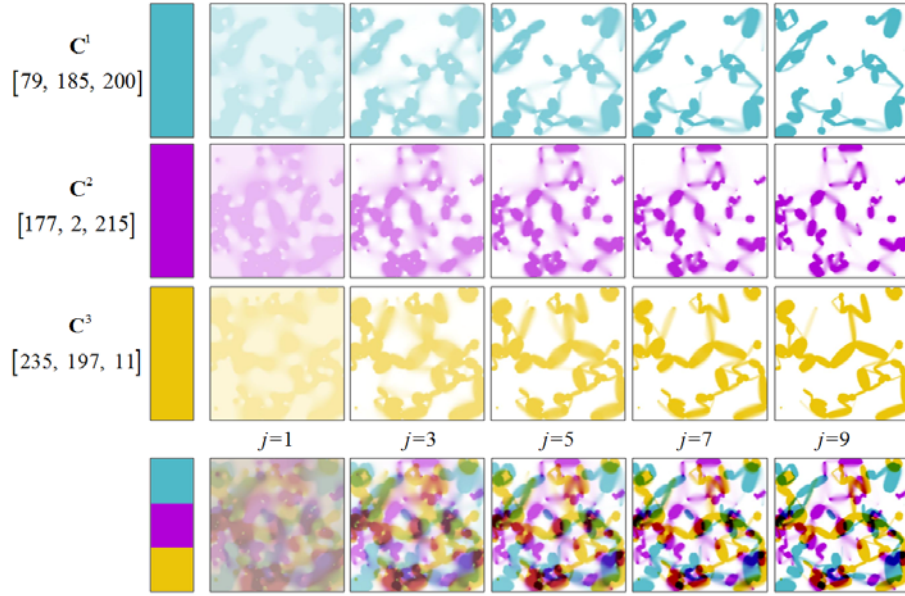


Figure 3.8 Superposed images based on the proposed color mixing rule in Eq. (3.20) (j : iteration number).

Finally, a technique for using a baseline image is proposed. The main difference between the case with a baseline image and the case without one is determining how to assign the conductivity value (k^e) to each finite element. When there is no baseline image, the same value of $k^e = 1$ is assigned to all elements. On the other hand, the element conductivity value is dependent on its brightness when a baseline image is used. Specifically, the value v^e ($0 \leq v^e \leq 1$) appearing in the HSV (hue-saturation-value) model that can be determined for the e -th finite element is directly used as its conductivity value k^e :

$$k^e = v^e \quad (3.21a)$$

$$\text{or } k^e = 1 - v^e \quad (3.21b)$$

Unlike the case without a baseline image, k^e 's are non-uniformly distributed in the canvas region or the virtual plate. If Eq. (3.21a) is used, for example, optimal heat path are formed mainly near or on the elements having large k^e values.

3.3.2 The effects of parameter group \mathbf{P}_B

Parameters belonging to \mathbf{P}_B are needed to define the virtual heat transfer system. In this subsection, we will examine how images are affected by the values of the parameters in \mathbf{P}_B . The canvas region or the virtual plate where heat transfer takes place is discretized into 400×400 finite elements in all test problems discussed.

First, let us consider the effects of the distance between a heat source (starting point) and a heat sink (ending point) on image generation. Figure 3.9 shows the effect of the source-sink distance on obtained images. Here, we only consider a single source and a single sink in order to clearly demonstrate the effects. All parameters other than the distance are the same for all cases considered in Fig. 3.9.

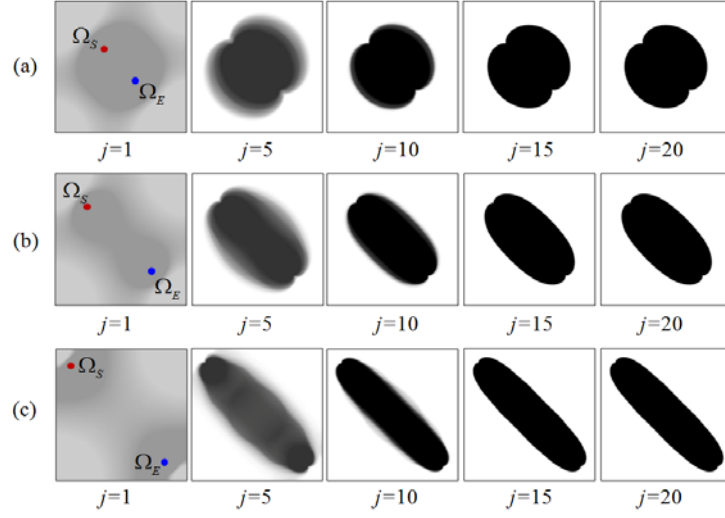


Figure 3.9 The effect of the source-sink distance on generated image. The canvas region is discretized by 400×400 elements. ($M = 0.3$, $Q^* = 1$, $h^* = 1$, $p = 3$, $n_{iter} = 20$) The height and width of every element are unity (units are ignored). (a) Distance = $2\sqrt{2}$, (b) Distance = $100\sqrt{2}$, (c) Distance = $300\sqrt{2}$.

Because the use of more mass reduces the value of the objective function $\Pi = \boldsymbol{\theta}^T \mathbf{K} \boldsymbol{\theta}$, the given mass is fully used. Therefore, the optimized path widens as the distance between the sink and the source is decreases. Slender paths can be found when the distance is large.

Next, the effects of the numbers of heat sinks and sources are examined. Fig. 3.10 shows the images obtained for a single source with a varying number of sinks while Fig. 3.11 shows the images obtained for a single sink with a varying number of sources.

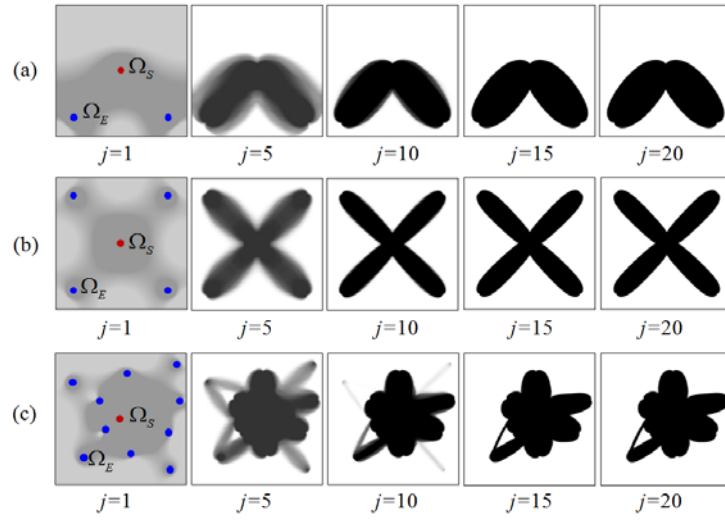


Figure 3.10 The effects of varying the number of heat sinks (ending points) for a single heat source (starting point) ($M = 0.3$, $Q^* = 1$, $h^* = 1$, $p = 3$, $n_{iter} = 20$) (a) $N^E = 2$, (b) $N^E = 4$, (c) $N^E = 10$

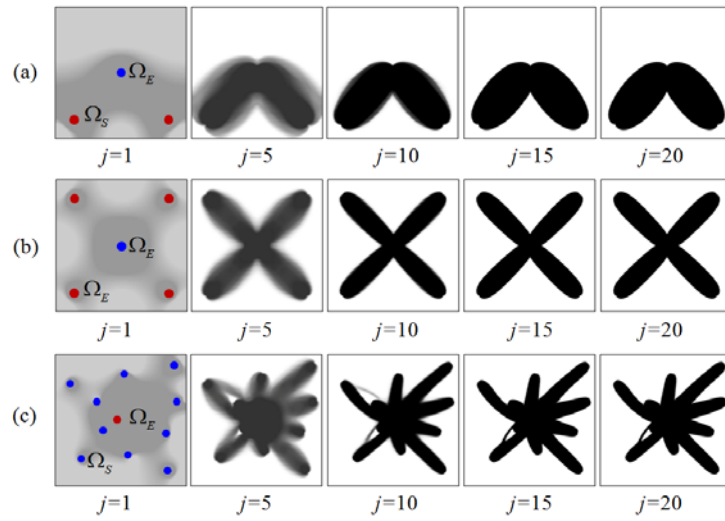


Figure 3.11 The effects of varying the number of heat sources (starting points) for a single heat sink (ending point) ($M = 0.3$, $Q^* = 1$, $h^* = 1$, $p = 3$, $n_{iter} = 20$) (a) $N^S = 2$, (b) $N^S = 4$, (c) $N^S = 10$

A comparison of the results in Fig. 3.10 and Fig. 3.11 illustrates the role of starting and ending points in image generation. Although one cannot distinguish between starting and ending points just by seeing the obtained images, the difference in the two figures can be explained by the formulated thermal compliance minimization. Because the objective function $\Pi = \boldsymbol{\theta}^T \mathbf{K} \boldsymbol{\theta}$ can be rewritten by using Eq. (3.5) as

$$\Pi = \mathbf{F}^T \boldsymbol{\theta} , \quad (3.22)$$

where \mathbf{F} involves only the heat source Q as defined in Eq. (3.11). Accordingly, all source points (starting points) must be connected to the sink point (ending point) in Fig. 3.10. Otherwise, the incoming heat at the source points cannot escape from the plate, yielding high temperature at the source points. On the other hand, not all sink points need to be connected to the source point because only a few heat paths would be sufficient to effectively transfer heat from a source to the sinks.

Next, numerical experiments are performed by varying the relative magnitudes of sinks and sources. Fig. 3.12 shows the results with varying ratios of the magnitudes of two sinks while Fig. 3.13 shows the results with varying ratios of the magnitudes of two sources.

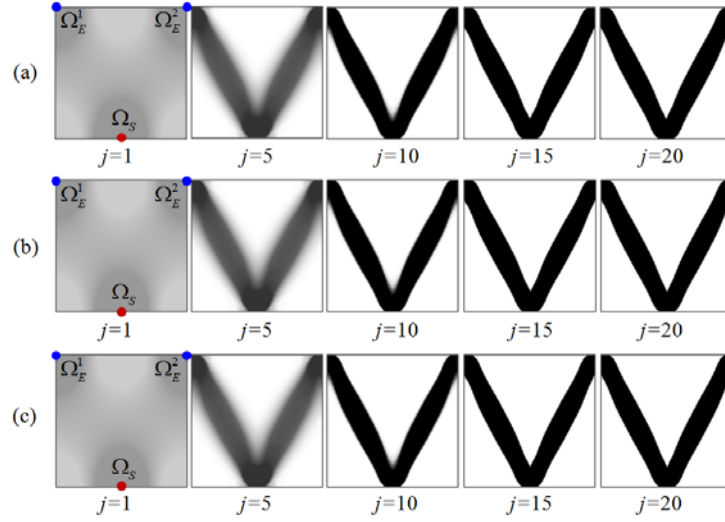


Figure 3.12 Results of numerical experiments with varying ratios of the magnitudes of two sinks for a single source of fixed magnitude. ($M = 0.3$, $Q^* = 1$, $p = 3$, $n_{iter} = 20$) (a) $h_1^* : h_2^* = 1:1$, (b) $h_1^* : h_2^* = 3:1$, (c) $h_1^* : h_2^* = 5:1$

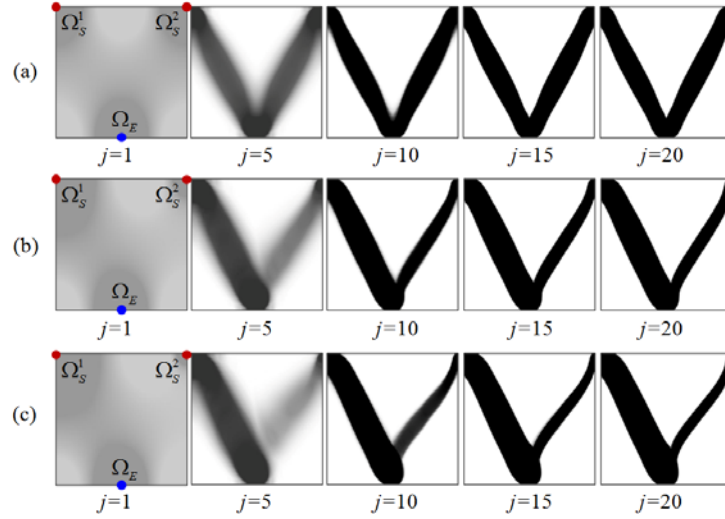


Figure 3.13 Results of numerical experiments with varying ratios of the magnitudes of two sources for a single sink of fixed magnitude. ($M = 0.3$, $h^* = 1$, $p = 3$, $n_{iter} = 20$) (a) $Q_1^* : Q_2^* = 1:1$, (b) $Q_1^* : Q_2^* = 3:1$, (c) $Q_1^* : Q_2^* = 5:1$

The difference between the images in Fig. 3.12 and those in Fig. 3.13 is also due to the different physical characteristics of sinks and sources. For instance, the heat coming through Ω_S dominantly flows to Ω_E^1 , which has a larger h^* value (see Fig. 3.12) because Ω_E^1 can remove heat from the system more efficiently than Ω_E^2 .

The final experiments are conducted with varying numbers of sinks and sources (N^E, N^S). The experimental results for three different cases are shown in Fig. 3.14. The more N^S and N^E are used, the finer the obtained images are. The results indicate that control of N^S and N^E makes a significant difference in the obtained images.

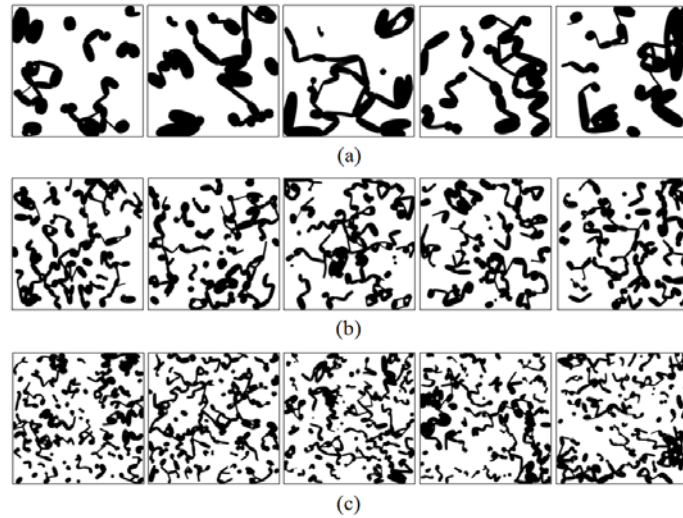


Figure 3.14 Experiments with different numbers of sinks and sources. ($M = 0.3$, $Q^* = 1$, $h^* = 1$, $p = 3$, $n_{iter} = 20$) (a) $(N^S, N^E) = (25, 25)$, (b) $(N^S, N^E) = (100, 100)$, (c) $(N^S, N^E) = (200, 200)$ (the sink and source locations are randomly assigned).

3.3.3 The effects of parameter group \mathbf{P}_C

Parameters belonging to group \mathbf{P}_C are those needed in the topology optimization algorithm. Since the effects of \mathbf{P}_C on structural engineering problems are relatively well-documented [63], they will be summarized briefly here for the sake of completeness. First, the effects of n_{iter} (maximum iteration number allowed) are considered for the simplest case of a single source and a single sink.

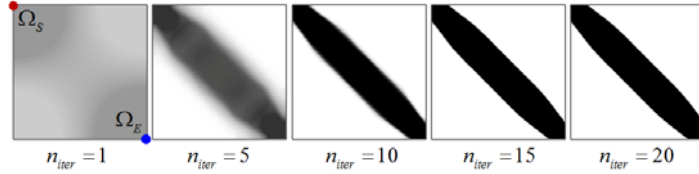


Figure 3.15 Images obtained with varying maximum iteration numbers.

$$(M = 0.3, Q^* = 1, h^* = 1, p = 3)$$

Due to the characteristics of the standard density-based topology optimization algorithm (with $p > 1$), distinct images are obtained as n_{iter} becomes large. The influence of the mass constraint ratio is shown in Fig. 3.16. The greater the allowed mass, the thicker the stroke (the heat path) becomes.

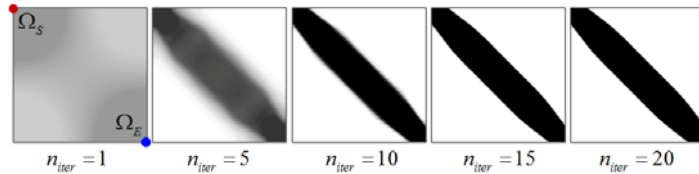


Figure 3.16 The effects of the mass constraint ratio on the obtained images.

$$(Q^* = 1, h^* = 1, p = 3, n_{iter} = 20)$$

Finally, the effects of p (penalty exponent) on the obtained images are examined in Fig. 3.17. If $p > 1$, then distinct images be obtained but local optimal results may be obtained [63]. On the other hand, blurred images can be obtained if $p = 1$. Although blurred images should be avoided in practical engineering applications, they can give an impression of ink-and-wash painting. In fact, this may also be an additional advantage of using the variational art algorithm.

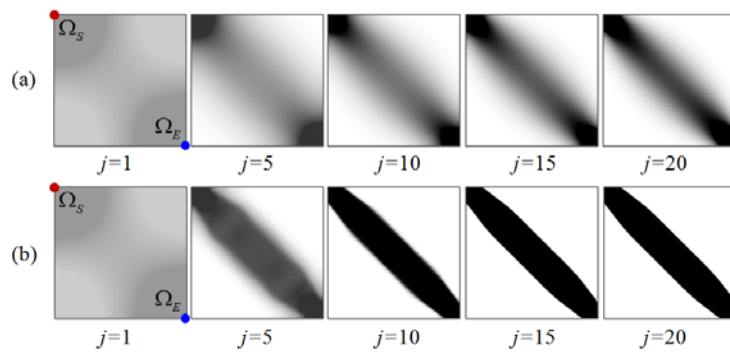


Figure 3.17 The effects of the penalty exponent on the obtained images.
 $(M = 0.3, Q^* = 1, h^* = 1, n_{iter} = 20)$ (a) $p = 1$, (b) $p = 3$

3.4 Summary

By transforming the topology optimization method into the variational art algorithm, we developed a new automated algorithm to generate color images. A virtual physical system describing the heat transfer phenomenon from heat sinks and sources was created to mimic brush strokes of a painter. Various impressions of the images created by the algorithm were realized by controlling the parameters appearing in the topology optimization problem to find optimal heat paths in the virtual system. Because no real engineering problem is involved here, some constraints on the parameters of topology optimization can be removed and even arbitrarily set. Due to this freedom, it was possible to obtain images having an impression of an ink-and-wash painting. The artistic virtue of images that are created by the variational algorithm may be debatable, but this investigation showed a new possibility of expanding the topology optimization method, a purely engineering method, beyond the engineering realm to an art/design realm. Only a heat transfer system with certain boundary conditions was investigated as a virtual system in this study. Work is in progress to develop virtual systems such as those dealing with wave propagation, structural compliance, etc., which could yield considerably different images.

Chapter 4

Conclusion

In this thesis, topology optimization method has been applied into two kinds of non-conventional applications. The first is the path planning algorithm of a mobile robot and the second is the variational art algorithm. In general, there has been a lot of research to broaden the scope of the applications of topology optimization technique. Such studies, however, were limited to areas of structural design associated with a variety of physical systems. As far as I know, the researches about topology optimization applied to the field of novel engineering instead of the traditional engineering disciplines related to the mechanics are extremely rare. Moreover, there is no case where the method has been successfully used for the non-engineering field such as visual design. The originality and contributions of this thesis exist in that point.

The topology optimization of the heat path design is very important properties that are effective to the path planning. Essentially, the method mathematically mimics the physical heat transfer phenomenon that thermal energy incoming to the system should necessarily flow out along the path that most efficient. Moreover, topology optimization methodology has been developed to find that path exactly. The method suggested in this thesis was started from this observation and has effectively addressed a variety of path planning problems. For example, we has addressed the original problem that plans the path avoiding obstacles, smoothing path problem that plans a continuous curvature

path for a car-like robot, and long range routing problem that plans the path in huge real terrain. The results are very encouraging. Compared with conventional approaches, the proposed method has various advantages. Among them, the followings are representatives. The first is that it is not affected by the complexities of the map. For example, the computation time is necessary affected only the size of the map. The complexities of a map such as the number, shape, and density of obstacles never effect. The second is that the map building and re-building is very easy. Our method can use the DEM(digital elevation map) directly. And also, different from the conventional graph map representation, new obstacles can be easily added to the previous map without re-building of an entire map, which is very hard work in general. The third is the good quality of a path. Because that topology optimization find the optimal path using optimization technique, it is easy to implement finding some specific path. Although, in this thesis, only shortest path finding problems are solved by using the minimization of thermal compliance, the possibility to find various optimal paths by formulating the suitable objective functions is abundant. And also, the resultant path obtained from the proposed method is constructed by the consecutive of finite elements. In other words, compared to the graphical paths being composed with the vertices and edges, the information of the path is abundant and exact. This quality of the path is very useful to the smoothing technique interpolating the path as smooth curve, which is executed secondly after obtaining the path. On the other hand, proposed method has disadvantages also. The main disadvantage is the high cost of computation time. As mentioned earlier, compared to conventional graph search algorithms, the computation time is long. This is not avoidable property originated from the FEM (finite element

method) used in the proposed method. However, although it is hard to make better than the graph search algorithms, there is a change to improve. For example, the parallel processing widely used in various image filtering can be applied to it. And it has been demonstrated already in this thesis that the matrix assembly time can be reduced by parallel processing.

The variational art algorithm is the convergence research of engineering and art. Its motivation is originated from the study applying topology optimization into the path planning problem. Phenomenally, the path is a line. In other words, path planning is to draw the line. And drawing a line is fundamentals of image creations. Moreover, by appropriately adjusting various parameters, novel images can be created. Practically, the various artistic images can be created. As mentioned at the beginning of paragraph, the variational art algorithm is the convergence research. So, the value of it should be recognized from not only engineering but also art. Because it is not suitable to recognize the artistic values in this thesis, it is not mentioned in this thesis. However, it should be mentioned that the variational art had won at the competition of 2011's Art Sapce, Seogyo and the artworks had been exhibited at Art Space, Seogyo from 11 to 19, November, 2011. Some examples are added in Appendix B. From the point of engineering view, the properties of the parameters affecting the image are suggested and studied in the text. And also some different formulation of color mixing techniques is suggested. Compared to the various image processing tools used conventionally, the variational art algorithm has originality that images are created in by the mathematical optimization process and physical simulation of heat transfer. From this reason, the user (artist) cannot control the resultant image perfectly.

From some point of view, this is a disadvantage. However, this study is just the beginning and the controllability of the resultant artwork will be improved in the near future.

Bibliography

- [1] M.P. Bendsøe, N. Kikuchi, Generating optimal topologies in structural design using a homogenization method. *Comp. Meth. Appl. Mech. Engng.* 1988, 71(2): 197-224.

- [2] L.A. Krog, K. Tuck, Topology optimization of aircraft wing box ribs, AIAA 2004-4481, 2004

- [3] B.C. Chen, N. Kikuchi, Topology optimization with desing-dependent loads, *Finite Elements in Analysis and Design*, 2001, 37: pp 57-70

- [4] H.C. Gea, J. Luo, Topology optimization of structures with geometrical nonlinearities, *Computer and Structures* 2001, 79: 1977-1985

- [5] P. Duysinx, M.P. Bendsøe, Topology optimization of continuum structures with local stress constraints, *Numerical Methods in Engineering*, 1998, 43: 1453-1478.

- [6] G.H. Yoon, Y.Y.Kim, Eelement connectivity parameterization for topology optimization of geometrically nonlinear structures, *Int. J. Solid Struct.*, 2005, 42: 1983-2009.

- [7] J.C. Ryu, Y.Y. Kim, Density-dependent shape function approach for trouble-free topology optimization for heat transfer problems including

side convection, in: Proceedings of 7th World Congress on Structural and Multidisciplinary Optimization, Seoul, Korea, May 21–25, 2007.

- [8] A. Iga, S. Nishiwaki, K. Izui, M. Yoshimura, Topology optimization for thermal conductors considering design-dependent effects, including heat conduction and convection, *Int. J. Heat Mass Transfer*, 2009, 52: 2721-2732
- [9] T.E. Bruns Topology optimization of convection-dominated, steady-state heat transfer problems, *Int. J. Heat Mass Transfer*, 2007, 50: 2859-2873
- [10] T. Gao, W.H. Zhang, J.H. Zhu, Y.J. Xu, D.H. Bassir Topology optimization of heat conduction problems involving design-dependent heat load effect, *Finite Elements in Analysis and Design*, 2008, 44: 805-813
- [11] A. Gersborg-Hansen, O. Sigmund, R.B. Haber, Topology optimization of channel flow problems, *Struct. Multidiscp. Optim.* 2005, 30(3): 181-192.
- [12] T. Borrvall, J. Petersson, Topology optimization of fluids in stokes flow, *Int. J. Numer Methods Fluids*, 2003, 41: 77-107.
- [13] J.K. Guest, J.H. Prevost, Topology optimization of creeping fluid flows using a Dracy-Stokes finite element, *Int. J. Numer Methods Engineering*, 2006, 66: 461-484

- [14] S.H. Cho, Y. Kim, Y.Y.Kim, The optimal design and experimental verification of the bias magnet configuration of a magnetostrictive sensor for bending wave measurement. *Sens. Actuators A: Physical*. 2003, 107: 225-232.
- [15] W. Kim, J.E. Kim, Y.Y. Kim . Coil configuration design for the Lorentz force maximization by the topology optimization method: Applications to optical pickup coil design, *Sens. Actuators: Phys. A* 2005, 121: 221-229
- [16] Y.Y. Kim, W. Kim, Yoke topology optimization of the bias magnetic system in a magnetostrictive sensor. *KSME (Korean Society of the Mechanical Engineers) Journal A (in Korean)* 2004, 28(7): 923-929
- [17] G.H. Yoon, J.S. Jensen, O. Sigmund, Topology optimization of acoustic-structure interaction problems using mixed finite element formulation, *Int. J. Numer. Meth. Eng.*, 2007, 70:1049-1075
- [18] J.S. Lee, Y.Y. Kim, J.S.Kim, Y.J.Kang Two-dimensional poroelastic acoustic foam shape design for absorption coefficient maximization by topology optimization method, *J. Acoust. Soc. Am.*, 2008, 123: 2094-2106
- [19] Y.J. Kim, Y.Y.Kim, Solid-perforated panel layout optimization by topology optimization based on unified transfer matrix, *J. Acoust. Soc. Am.*, 2010, 128: 1777-1788
- [20] Y.Y. Kim, G.W. Jang, J.H. Park, J.S. Hyun, S.J. Nam, Configuration

design of rigid link mechanisms by an optimization method: a first step, in: Proc. IUTAM Symp. On Topological Design Optimization of Structures, Machines and Materials, Springer, pp 251-260, 2005

- [21] K.H. Sun, Y. Y. Kim, "Design of Magnetoelectric Multiferroic Heterostructures by Topology Optimization ," Journal of Physics D: Applied Physics, 2011, 44(18):185003-1~8
- [22] S.K. Koh, G. Liu, W.H. Zhu, A continuous protein design model using artificial power law in topology optimization, J. Mech. Des., 131(2009):
- [23] S.K. Koh, G.K. Ananthasuresh, S. Vishveshwara, A deterministic optimization approach to protein sequence design using continuous models, Int. J. Robot. Res., 2005, 24: 109-130.
- [24] J.C. Ryu, F.C. Park, Y.Y. Kin, Mobile robot path planning algorithm by equivalent conduction heat flow topology optimization, Struct. Multidisc. Opt. in print (2012)
- [25] H. Choset, K.M. Lynch, S. Hutchinson, G. Kantor, W. Burgard, L.E. Kavraki, S. Thrun, Principles of robot motion: theory, algorithm, and implementations, The MIT Press, Cambridge, 2005.
- [26] S. Thrun, W. Burgard, Probabilistic robotics, The MIT Press, Cambridge, 2005.

- [27] S.M. LaValle, *Planning algorithm*, Cambridge Uni. Press, New York, 2006.
- [28] P. Svestka and M.H. Overmars, Probabilistic path planning, *Rob. Mot. Plan. Cont.*, 1998, 229:255-304.
- [29] S. Rodriguez, S. Thomas, R. Pearce, N.M. Amato, RESAMPL: a region-sensitive adaptive motion planner, In: *Proc int wkshp on Alg. Found of rob*, New York City, NY, 2006.
- [30] T.L. Perez, A simple motion-planning algorithm for general robot manipulators, *J Rob. Auto.* 1987, 3: 224-238.
- [31] O. Khatib, Real-time obstacle avoidance for manipulators and mobile robots, *Int. J. Rob. Research*, 1986, 5(1): 90-98.
- [32] E.D. Koditchek, E. Rimon, Robot navigation functions on manifolds with boundary, *Advan. App. Math.* 1990, 11(4): 412-442.
- [33] O.J. Kim, P. Khosla, Real-time obstacle avoidance using harmonic potential functions, *IEEE Trans. Rob. Auto.* 1992, 8(3): 338-349.
- [34] A. Masoud, S. Masoud, M. Bayoumi, Robot navigation using a pressure generated mechanical stress field: the biharmonic potential approach. *Proc. IEEE Int. Conf. Rob. Auto.*, San Diego, 1994, pp.124-129.

- [35] L. Singh, S. Harry, J. Wen, Real-time robot motion control with circulatory fields, In: Proc. IEEE Int. Conf. Rob. Auto., Minneapolis, 1996, pp. 2737-2742.
- [36] D. Keymeulen, J. Decuyoeer, The fluid dynamics applied to mobile robot motion: the steam field method, Proc. IEEE Int. Conf. Rob. Auto., Sand Diego, 1994, pp. 378-385.
- [37] C. Louste, A. Liegeois, Near optimal robust path planning for mobile robots: the viscous fluid method with friction, J. Intel. Rob. Sys. 2000, 27: 99-112.
- [38] G.K. Schmidt, K. Azarm, Mobile robot navigation in a dynamic world using an unsteady diffusion equation strategy, In: Proc. IEEE Int. Conf. Intel. Rob. Sys., Raleigh, 1992, pp. 642-647.
- [39] D.K. Pai and L.M. Reissell, Multiresolution rough terrain motion planning, IEEE Trans. Rob. Auto. 1998, 14(1): 19-33.
- [40] P. Tompkins, A. Stentz, and D. Wettergreen, Global path planning for mars rover exploration, IEEE AC paper #1339, 2004.
- [41] V. Hosagrahara, K Tamminana, and G. Sharma, Accelerating finite element analysis in MATLAB with parallel computing, MATLAB Digest, The MathWorks, Inc. 2010

- [42] A.M. Noll, The digital computer as a creative medium, *spectrum*, IEEE, 1967, 4(10):89-95.
- [43] C. Csuri, Computer graphics and art, *Proceedings of the IEEE*, 1974, 62(4):503-515.
- [44] B.B. Mandelbrot, Fractals and an art for the sake of science, Leonardo. Supplemental Issue, *Computer Art in Context: SIGGRAPH '89 Art Show Catalog*, 1989, 2: 21-24.
- [45] J. McCormack, Open problem in evolutionary music and art, *APPLICATIONS OF EVOLUTIONARY COMPUTING*, Lecture Notes in Computer Science, 2005, 3449: 428-436.
- [46] K. Sims, Artificial evolution for computer graphics, *Computer Graphics*, 1991, 25(4): 319-328.
- [47] E. den Heijer, A.E. Eiben, Comparing aesthetic measures for evolutionary art, *APPLICATIONS OF EVOLUTIONARY COMPUTING*, Lecture Notes in Computer Science, 2010, 6025: 311-320.
- [48] A. Bastanfard, H. Mansourifar, A novel decorative islamic star pattern generation algorithm, In: 2010 International Conference on Computational Science and Its Applications (ICCSA), pp. 111-117.
- [49] R. Alexander, Mycelium, < <http://onecm.com/projects/mycelium> >, 27

March 2012 online access.

[50] Nervous System, < <http://n-e-r-v-o-u-s.com/index.php> >, 27 March 2012 online access.

[51] J.E. Sabin, P.L. Jones, < <http://www.sabin-jones.com/arselectronica.html> >, 27 March 2012 online access.

[52] J. Giesbrecht, Global path planning for unmanned ground vehicles, Technical Memorandum, DRDC, Suffield, CA, 2004.

[53] Z.Y. Guo, X. Cheng, Z. Xia, Least dissipation principle of heat transfer potential capacity and its application in heat conduction optimization, Chinese Science Bulletin, 2003, 48(4): 406-410

[54] Y. Zhang, S. Liu, Design of conducting path based on topology optimization, Heat and Mass Transfer, 2008, 44: 1217-1227.

[55] F.P. Incropera, D.P. DeWitt, Fundamental of heat and mass transfer. 5-th edn., John Willey & Sons, New York, 2002.

[56] Y. Wang, G.S. Chirikjian, A new potential field method for robot path planning, In: Proc. IEEE Int. Conf. Rob. Auto., San Francisco, pp. 997-982.

[57] R.J. Yang, C.H. Chuang, Optimal topology design using linear

- programming. *Comp. Struct.*, 1994, 52: 265-275.
- [58] M. Stople and K. Svanberg, An alternative interpolation scheme for minimum compliance topology optimization, *Struct. Multidisc. Optim.* 2001, 22: 116-124.
- [59] K. Yang and S. Sukkarieh, An analytical continuous-curvature path-smoothing algorithm, *IEEE Trans. Rob.* 2010, 26(3):561-568
- [60] D.J. Walton and D.S. Meek, A controlled clothoid spline, *Comp. Graph.*, 2005, 29: 353-363
- [61] K.J. Bathe, *Finite element procedures*, Prentice Hall, New Jersey, 1996.
- [63] M.P. Bendsøe, O. Sigmund, *Topology optimization theory, methods and applications*. Springer, New York, 2003
- [64] M.P. Bendsøe, O. Sigmund, Material interpolation schemes in topology optimization, *Arch. Appl. Mech.* 1999, 69: 635-654
- [65] K.K. Choi, N.H. Kim, *Structural Sensitivity Analysis and Optimization 1: linear system*, Springer, New York, 2005.
- [66] K. Svanberg, The method of moving asymptotes - a new method for structural optimization, *Int. J. Numer. Meth. Eng.*, 1987, 24: 359-373

- [67] O. Sigmund, J. Petersson, Numerical instabilities in topology optimization: a survey on procedures dealing with checkerboards, mesh-dependencies and local minima, *Struct. Optim.*, 1998, 16: 68-75.
- [73] O. Sigmund, Design of material structures using topology optimization, Ph.D. Thesis, Department of Solid Mechanics, Technical University of Denmark, 1994.

Appendix A:

Topology Optimization Formulation

This section describes the topology optimization formulation of the problem mentioned in previous section. The general objective of topology optimization of a thermal structure design is to find the distribution of matter, or in other words, the distribution of thermal conductivity that allows more efficient heat transfer. For this, material property interpolation method [64] is most widely used. In that method, the thermal conductivity of e -th element (k_e) is interpolated as follows:

$$k_e = k_0 x_e^p \quad (\text{A.1})$$

In Eq. (A.1), x_e , k_0 and p are, respectively, design variable of a element, nominal thermal conductivity, and penalty exponent. x_e is defined as the following range of values.

$$0 < \varepsilon \leq x_e \leq 1 \quad (\varepsilon = \text{very small value}) \quad (\text{A.2})$$

Topology optimization formulation of thermal structure design is formulated as follow: [63]

$$\underset{(\gamma_1, \gamma_2, \gamma_3, \dots, \gamma_{Ne})}{\text{minimize}} \quad \Pi = \mathbf{F}^T \boldsymbol{\theta} = \boldsymbol{\theta}^T \mathbf{K} \boldsymbol{\theta} \quad (\text{A.3})$$

$$\sum_{e=1}^{Ne} \gamma_e m_e - M_0 \leq 0 \quad (\text{A.4})$$

$$0 < \varepsilon \leq \gamma_e \leq 1 \quad (e = 1, 2, \dots, Ne; \varepsilon = \text{very small value}) \quad (\text{A.5})$$

In Eq. (A.4) and Eq. (A.5), γ_e is used as the symbol that represents the design variable. m_e and M_0 , respectively, means nominal mass of each element and total mass fraction allowed to use. The objective function (Π) of Eq. (A.3) indicates thermal compliance which means the dissipation of heat transfer potential capacity. [53] More details regarding thermal compliance will be described in Section 2.1.2.

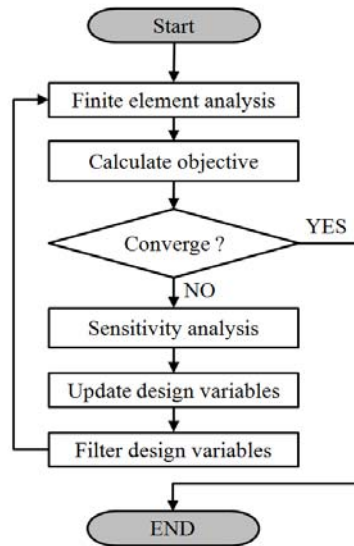


Figure A.1 Flow chart of topology optimization of thermal structure

Figure A.1 shows the flow chart of topology optimization of thermal structure. After calculating the objective function, then the convergence criteria is

evaluated. If the convergence criteria are not satisfied, until the convergence criteria are satisfied, the sensitivities are evaluated and design variables are updated. By using adjoint variable method [65], the sensitivity is calculated as follow:

$$\frac{\partial \Pi}{\partial \gamma_e} = (\boldsymbol{\theta}^e)^T \frac{\partial \mathbf{K}^e}{\partial \gamma_e} (\boldsymbol{\theta}^e) \quad (\text{A.6})$$

In this research, Optimal Criterion (OC) is used as optimization algorithm. However, generally, Method of Moving Asymptotes (MMA) [66] is also usable. To avoid checker-board problem, mesh-independent filtering method suggested by Sigmund are used as follow:[67]

$$\frac{\overline{\partial \Pi}}{\partial \gamma_i} = \frac{\sum_{j=1}^{N_s} \frac{\partial \Pi}{\partial \gamma_j} \gamma_j (R - r_j)}{\sum_{j=1}^{N_s} \gamma_j (R - r_j)} \quad (\text{A.7})$$

Appendix B:

Exhibition and Artworks

B.1 Exhibition

Variational art algorithm presented in this thesis is a kind of convergence research of engineering technique and aesthetic visual art. This research had been studied by a project group named as “Project 33” consisting of an artist (H.K. Kim) and engineers (J.C. Ryu and Y.Y. Kim). For that reason, the aesthetic assessment has to be accompanied with the assessment of a technical value. However, it is hard to evaluate the aesthetic value of the artworks generated by variational art algorithm through objective indicators. So, we announce the fact that the artworks and project was nominated as one of the winners at the competition sponsored by Seoul Art Space “Seogyo”. (see. Fig. B.1 and B.2)

The exhibition under the theme of “Mass Production of Differences” was held at Seoul Art Space “Seogyo” from November 11 to November 19 in 2011. Some artworks displayed in the exhibition are presented in Section A.2.

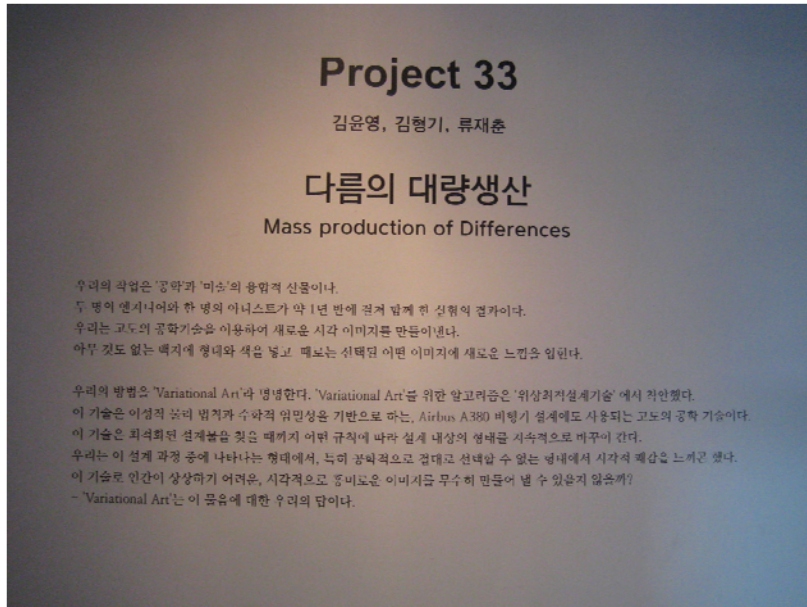


Figure B.1 Exhibition title and description

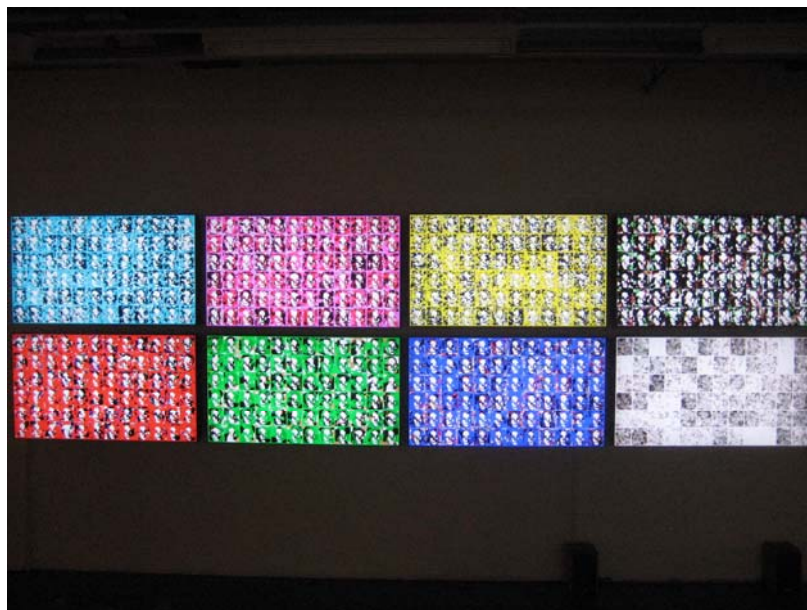


Figure B.2 Media art displayed in exhibition

B.2 Artworks



Figure B.3 Body series No. 3, Project 33, 2011

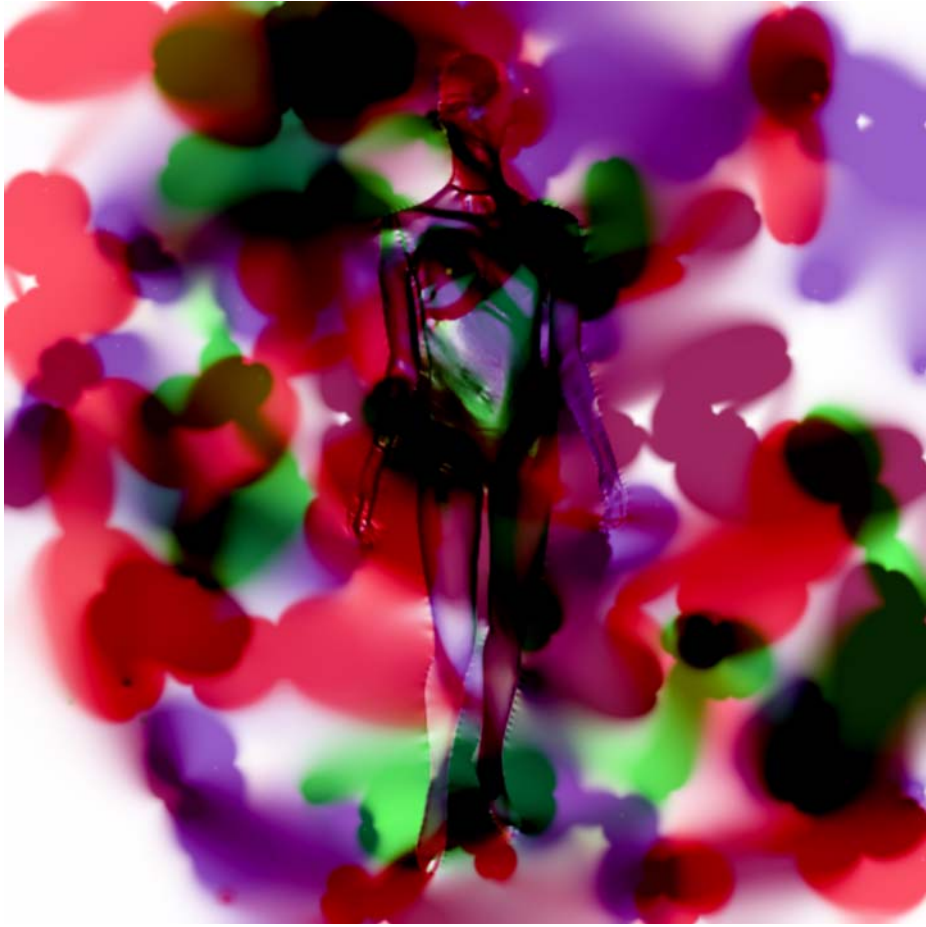


Figure B.4 Body series No. 12, Project 33, 2011



Figure B.5 Body series No. 28, Project 33, 2011



Figure B.6 Drawing series No. 2, Project 33, 2011



Figure B.7 Drawing series No. 5, Project 33, 2011



Figure B.8 Drawing series No. 9, Project 33, 2011



Figure B.9 Figure series No. 3, Project 33, 2011



Figure B.10 Figure series No. 8, Project 33, 2011

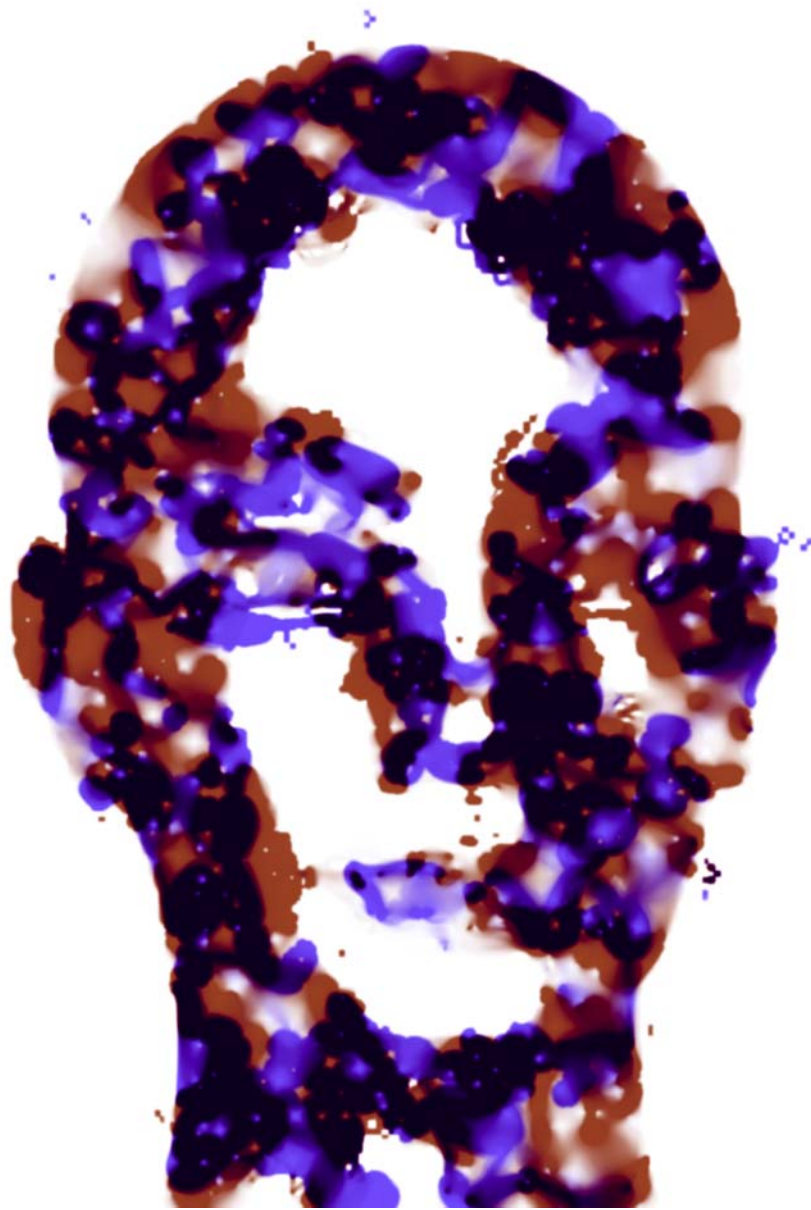


Figure B.11 Figure series No 17, Project 33, 2011



Figure B.12 Skeleton series No. 7, Project 33, 2011



Figure B.13 Skeleton series No. 65, Project 33, 2011



Figure B.14 Skeleton series No. 72, Project 33, 2011



Figure B.15 Manikin series No. 4, Project 33, 2011



Figure B.16 Manikin series No. 8, Project 33, 2011



Figure B.17 Manikin series No. 10, Project 33, 2011

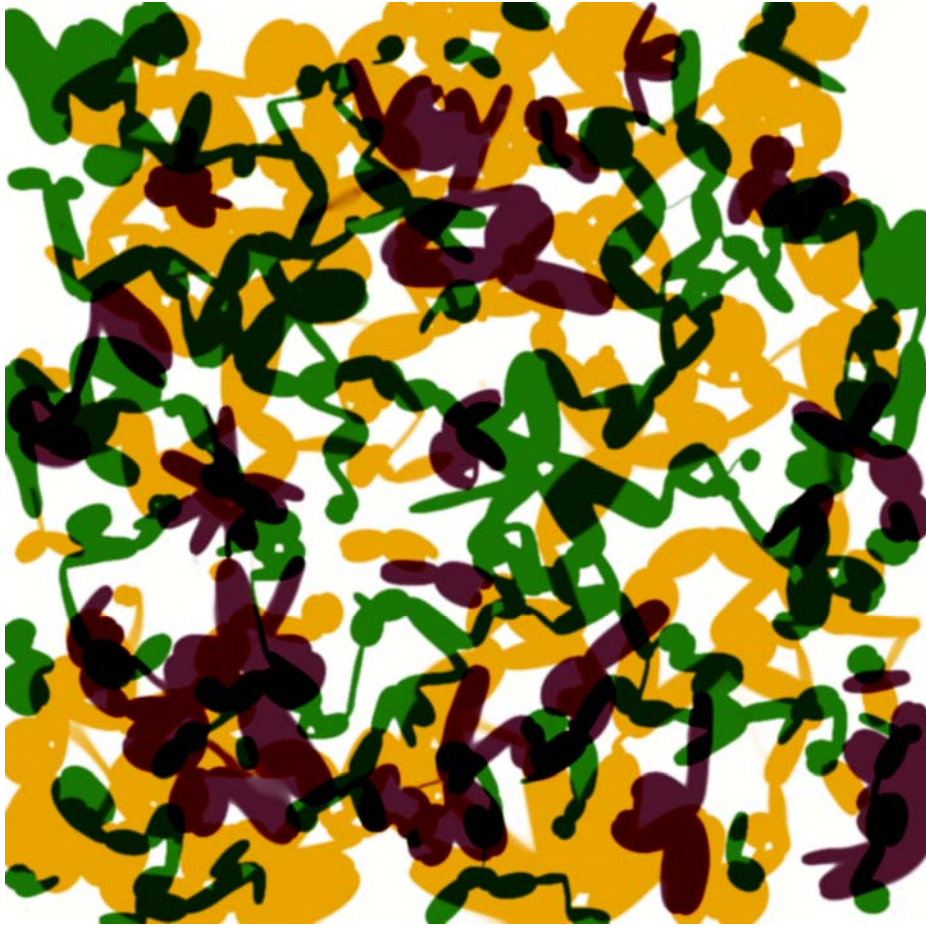


Figure B.18 Abstract series No. 4, Project 33, 2011

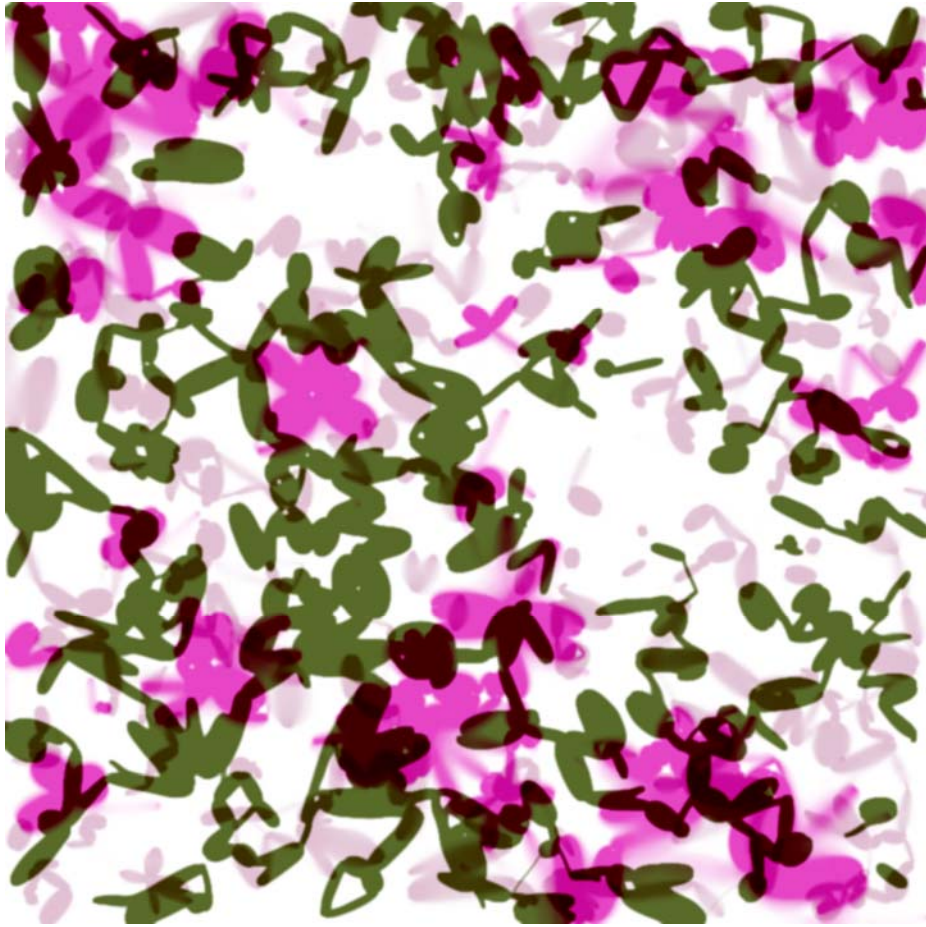


Figure B.19 Abstract series No. 12, Project 33, 2011

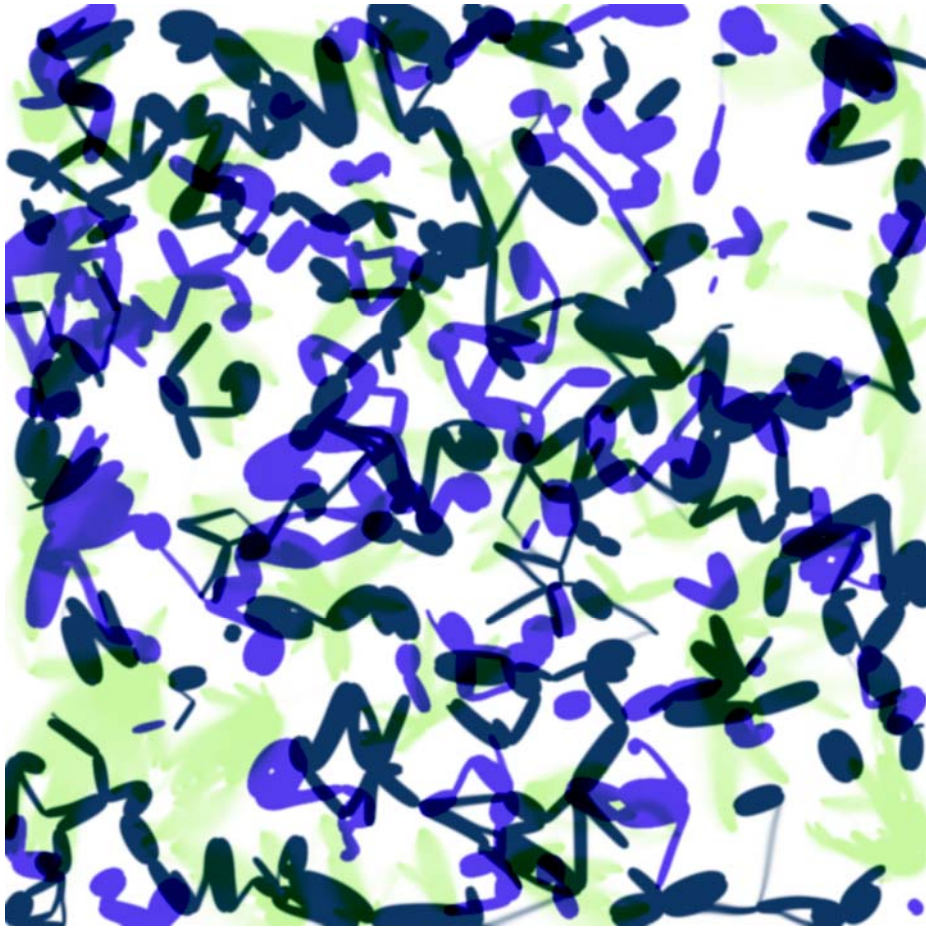


Figure B.20 Abstract series No. 25, Project 33, 2011



Figure B.21 Figure series II No. 3, Project 33, 2011



Figure B.22 Figure series II No. 11, Project 33, 2011



Figure B.23 Figure series II No. 24, Project 33, 2011

초 록

본 논문에서는 위상 최적 설계 기법을 응용하여 두 개의 독립적인 주제를 다룬다. 첫 번째 주제로 이동 로봇의 경로 계획 알고리즘을 제시하며, 두 번째 주제로는 변분 미술 알고리즘을 제시한다.

첫 번째 주제로, 다양한 장애물이 존재하는 공간에서 이동 로봇의 경로 계획 문제를 해결한다. 본 논문에서 제시하는 알고리즘은 열전달 현상과 위상 최적화 기법에 기반한다. 즉, 이동로봇의 시작점과 목표점을 열전달이 가능한 평판에서의 열 발생점과 열 소실점으로 정의하고, 경로 계획 문제를 열강성을 최소화하는 열전달 경로의 최적 설계문제로 정식화한다. 이 때, 경로 계획 문제의 장애물은 단열물질의 분포로 간주한다. 또한 더 나아가, 설계 영역의 열전도도를 다양하게 부여함으로써, 단순 장애물 회피 경로의 설계 문제뿐 아니라, 지형 조건을 고려한 경로 설계 문제를 해결한다. 본 논문에서는 실내 및 실외의 상황을 고려한 다양한 예제문제를 통해 제시하는 경로 계획 알고리즘의 실용성 및 타당성을 검증한다.

두 번째 주제로, 본 논문은 열전달 현상 및 변분법에 기반하여 미적으로 유의미한 시각 디자인 작품을 만들어내는 컴퓨터 알고리즘을 제시한다. 제시하는 변분 미술 알고리즘은 빈 화폭에 그림을 그리는 방법과 유사하다. 즉, 선과 평면을 그리는 과정을 2차원 평면에서 열 발생점과 열 소실점을 질량 제한 조건하에서

물질분포를 최적화 하는 과정으로 간주한다. 이러한 과정에는 다양한 변수들을 조절할 수 있으며, 이러한 변수의 조절이 결과 이미지에 어떠한 영향을 주는가를 확인한다. 덧붙여, 본 논문에서 제시된 알고리즘으로 창작된 작품들을 제시한다.

주요어: 위상 최적화, 열전달, 경로 계획, 변분 미술
학 번: 2007-30194

감사의 글

사랑하는 유진이와

항상 양말을 벗겨주던 꼬둥이에게

고마운 마음을 전합니다.

2012년 7월 24일

연구실에서

류 제 춘